Oceanic-like axial crustal high in the central Red Sea

Oceanic-like axial crustal high in the central Red Sea

Wen Shi[1], Neil C. Mitchell[1], Lara M. Kalnins[2], A.Y. Izzeldin[3]

[1]School of Earth and Environmental Sciences, The University of Manchester, Manchester M13 9PL, UK.

[2]School of GeoSciences, The University of Edinburgh, The King's Buildings, Edinburgh, EH9 3FE, UK.

[3]Awasconrc, Gereif W, H4, Bld 376, Khartoum, POB 410, Khartoum.

Address for correspondence: mjshiwen@gmail.com

Highlights:

- Deep seismic data reveal oceanic-like axial ridge beneath central Red Sea.
- Axial high is similar to those of hotspot-affected spreading centres.
- Bouguer anomalies predict low average density beneath axis.
- This low density implies thickened crust and/or low mantle density.
- Normal thickness predicted from Na8.0 implies recent transition from thinner crust.

Keywords: Red Sea, Ocean–continent transition, Oceanic crust, Seismic reflection, Potential field, Subsalt

Abstract

The Red Sea is an important example of a rifted continental shield proceeding to seafloor spreading. However, whether the crust in the central Red Sea is continental or oceanic has been controversial. Contributing to this debate, we assess the basement geometry using seismic reflection and potential field data. We find that the basement topography from seismically derived structure corrected for evaporite and other sediment loading has an axial high with a width of 70-100 km and a height of 0.8-1.6 km. Basement axial highs are commonly found at mid-ocean ridges affected by hotspots, where enhanced mantle melting results in thickened crust. We therefore interpret this axial high as oceanic-like, potentially produced by recently enhanced melting associated with the broader Afar mantle anomaly. We also find the Bouguer gravity anomalies are strongly correlated with basement reflection depths. The apparent density contrast necessary to explain the Bouguer anomaly varies from 220 kg m^{-3} to 580 kg m^{-3} with no trend with latitude. These values are too small to be caused primarily by the density contrast between evaporites and mantle across a crust of uniform thickness and density structure, further supporting a thickened crustal origin for the axial high. Complicating interpretation, only a normal to modestly thickened axial crust is predicted from fractionation-corrected sodium contents ($Na_{8.0}$), and the basement reflection is rugged, more typical of ultra-slow spreading ridges that are not close to hotspots. We try to reconcile these observations with recent results from seismic tomography, which show modest mantle S-wave velocity anomalies under this part of the Red Sea.

1.0 Introduction

The Red Sea is a young ocean basin transitioning from continental extension to seafloor spreading (e.g., Bonatti et al., 1981; Cochran and Martinez, 1988; Rihm and Henke, 1998). However, how far the central Red Sea (Figure 1) is through this transition to full seafloor spreading has been debated.

Bonatti (1985) suggested the central Red Sea is just at the point of transitioning from continental rifting to oceanic spreading. He proposed that the 'deeps' found in the central Red Sea are discrete seafloor spreading cells based on the presence of normal mid-ocean ridge basalt (MORB) sampled from them and their high amplitude magnetic anomalies. This contrasts with low amplitude anomalies outside the deeps, which were therefore assumed to overlie stretched continental crust (Ligi et al., 2011, 2012).

However, other evidence could support the interpretation of more established seafloor spreading in the central Red Sea. An extensive aeromagnetic survey revealed that there are low amplitude magnetic anomalies outside the 'deeps' aligned parallel to the ridge axis (Izzeldin, 1987; Rasul et al., 2015). LaBrecque and Zitellini (1985) showed with numerical modelling that such subdued anomalies could be produced by widely distributed dykes, lava flows, and sills, as occur in modern-day Afar. Low amplitudes may also have arisen from the slow spreading rate, the greater depth of basement and alteration under the evaporites (Augustin et al., 2014; Dyment et al., 2013; Izzeldin, 1987, 1989; Levi and Riddihough, 1986; Mitchell and Park, 2014). The 'deeps' are separated by inter-trough zones, which are shallower, lacking in strong magnetic anomalies compared to the 'deeps', and covered by evaporites that have flowed laterally and sediments across the axis. Based on seismic reflection, gravity and magnetic data, Izzeldin (1982, 1987) suggested the inter-trough zones are manifestations of less organized seafloor spreading and underlain by oceanic crust. Using multibeam sonar data, Augustin et al. (2014, 2016) also interpreted these zones as merely areas where the off-axis evaporites have flowed into the axis, obscuring the volcanic geomorphology. Seismic refraction data show the velocity of basement under the inter-trough zone between Nereus and Thetis deeps (Figure 1) is 6.86 km s^{-1} (Davies and Tramontini, 1970; Tramontini and Davies, 1969), which overlaps with velocities of oceanic crust elsewhere (6.7-6.9 km s^{-1}; Carlson, 2001, 2010). Further seismic refraction data collected by Egloff et al. (1991) along line PIII (Figure 2) also suggested the basement around the ridge axis is oceanic,

which transitions to stretched continental crustal velocities towards the coast of Sudan. Finally, free-air gravity anomalies derived from satellite altimeter data (Sandwell et al., 2014; Sandwell and Smith, 2009) reveal that anomalies along the spreading centre are segmented (Figure 2). Mitchell and Park (2014) and Augustin et al. (2016) suggested that this segmented pattern is similar to the segmentation observed at slow-spreading mid-ocean ridges elsewhere (e.g., the northern Mid-Atlantic Ridge) (Schouten et al., 1987; Sempéré et al., 1990). The rugosity of basement computed from these anomalies is similar to that of the similarly slow-spreading Mid-Atlantic Ridge (Shi et al., 2017).

Based on seismic reflection and potential field data, Izzeldin (1982, 1987) suggested that intermediate crust separates crust that is clearly continental near the coasts from that which is clearly oceanic around the axis. This area lies ~65-160 km from the ridge axis.

Young ocean basins such as the Red Sea offer opportunities to explore mantle and crustal processes at the transition from rifting to seafloor spreading. In particular, the rate and geometry of deformation may be important for how rapidly the rising mantle cools during this phase. This in turn affects the flux of melt produced by mantle decompression and where oceanic crust is first emplaced. Buck (1986) suggested that lateral temperature gradients in the asthenosphere produced by rifting could lead to more rapid upwelling, implying a greater initial melt flux. Alternatively, the surface rifting and lithospheric mantle thinning could be laterally offset (Hopper and Roger Buck, 1998), implying a different location of initial magma emplacement. Some of these and other issues affecting the initial melting are illustrated in the recent numerical geodynamic models of Harry and Bowling (1999), Corti et al. (2003), Fletcher et al. (2009), Jeanniot et al. (2016), Ros et al. (2017), and Armitage et al. (2018). However, the evidence needed to investigate these ideas from basins presently transitioning to seafloor spreading is limited as examples are rare and often complicated. For example, the Woodlark Basin is small, opening relatively fast (~60 mm yr^{-1}) and in a complicated tectonic

97 setting that is still evolving rapidly after the Ontong Java collision with the West Melanesian
98 Trench (Martinez et al., 1999; Weissel et al., 1982). The Gulf of California rift is opening highly
99 obliquely (e.g., Atwater and Stock, 1998; Lonsdale, 1989; Withjack and Jamison, 1986). The
100 Red Sea, in contrast, is opening slowly (~10-~16 mm yr^{-1}) and more nearly orthogonally (e.g.,
101 Chu and Gordon, 1998), so it provides an important example of mantle and crustal dynamics
102 of slow orthogonal rifting.

103 In the present study, we use 11 lines of industrial seismic reflection data from the central Red
104 Sea reported in Izzeldin (1982, 1987). We verify interpreted basement depths using Werner
105 deconvolution applied to magnetic anomalies and then correct those depths for isostatic
106 loading by the evaporites and other sediments. The basement geometry is found to reveal
107 axial highs similar in gross morphology to, though larger than, those of the Reykjanes Ridge,
108 with more rapid deepening with distance from the axis that cannot be explained by simple
109 subsidence. This leads us to favour an oceanic interpretation for the crust here, in which melt
110 production has recently increased, creating thicker crust which forms the axial high. We then
111 discuss what these results imply about the evolution of this section of the Red Sea rift and
112 broader implications.

113 **2.0 Tectonic setting**

114 2.1 Continental rifting and seafloor spreading in the northern and southern Red Sea

115 The Red Sea opening rate increases southward from ~10 mm yr^{-1} at 25.5°N to ~16 mm yr^{-1}
116 near 18°N with increasing distance from the Nubia/Africa spreading pole, which lies in the
117 Mediterranean (e.g., Chu and Gordon, 1998; DeMets et al., 1990; DeMets et al., 2010). The
118 extension of the Red Sea may have begun in the Eocene but became more established in the
119 Oligocene, associated with massive and rapidly erupted basalts in Ethiopia and southern
120 Yemen at approximately 30 Ma (Bosworth and McClay, 2001; Hofmann et al., 1997; Mohr,

1983; Omar and Steckler, 1995). These rapid eruptions have been attributed to the Afar plume penetrating the lithosphere (Furman et al., 2006; George et al., 1998; Richards et al., 1989).

The northern Red Sea, which is closer to the pole of opening and has experienced less extension than our study area (Figure 1), has been thought to be underlain by continental crust with a series of large crustal fault blocks interpreted from seismic velocity data and from magnetic and gravity anomalies (Cochran and Karner, 2007; Gaulier et al., 1986; Martinez and Cochran, 1988). If correct, this area may still be in late stage continental rifting (e.g., Cochran, 1983; Gaulier et al., 1988; Martinez and Cochran, 1988). In contrast, others have interpreted this region as underlain by oceanic crust on the basis of unpublished seismic and magnetic data (e.g., Dyment et al., 2013; Tapponnier et al., 2013). Using remote sensing, geochemical, and geochronological data, Sultan et al. (1992) carried out a plate reconstruction for the opening of the Red Sea and found a best match of pre-existing African and Arabian geologic features by juxtaposing present Red Sea coastlines. This has been interpreted as indicating that the entire Red Sea basin is underlain by oceanic crust (Bosworth et al., 1993). In addition, a few 'deeps' containing basalts are revealed in the northern Red Sea (e.g., Bonatti, 1985; Guennoc et al., 1988; Ligi et al., 2018; Pautot et al., 1984).

In the southern Red Sea, farther from the pole than our study area (Figure 1), seafloor spreading magnetic anomalies are clearly identifiable up to Chron 3A near the axial trough between 16°N and 19°N, suggesting that recognizable seafloor spreading began at least by 5 Ma (e.g., Cochran, 1983; Girdler and Styles, 1974; Phillips, 1970; Vine, 1966). Augustin et al. (2016) suggested that oceanic spreading likely began somewhat earlier, 8-12 Ma, based on spreading rates of Chu and Gordon (1998) and locations of volcanic ridges interpreted from multibeam sonar and vertical gravity gradient data. These are consistent with the spreading ages (8–12 Ma) discussed by Izzeldin (1987) and Augustin et al. (2014). In addition to the clear

anomalies in the centre of the basin, Girdler and Styles (1974) and Hall (1989) also interpreted the low magnetic anomalies over the southern Red Sea shelves as seafloor spreading magnetic stripes, suggesting the Red Sea was formed by two stages of seafloor spreading. Based on magnetic and gravity modelling constrained by the seismic refraction data of Gettings et al. (1986) and Mooney et al. (1985), Almalki et al. (2014) recently suggested that about 75 km of oceanic crust formed before Middle to Late Miocene (15–5 Ma) under the Farasan Bank (Figure 1), which supports a two-stage spreading evolution of the Red Sea. In contrast, Cochran (1983) argued that these magnetic anomalies result from a wide region of mafic diking and intrusions rather than a continuous oceanic crust of dykes and extrusives, because the anomalies have low amplitudes (less than 200 nT) and long wavelengths (20-50 km). A seismic refraction line shot across the Yemen margin by Egloff et al. (1991) was interpreted as showing that oceanic crust adjacent to the axis terminates southward of 16°N and that continental-type crust lies farther south as far as 14˚N.

2.2 Seismic tomographic studies encompassing the Red Sea

Seismic tomographic studies have found that S- and P-wave seismic velocities of the upper mantle adjacent to the Red Sea increase by up to a few percent from south to north with increasing distance from the Afar plume. Using body wave travel time tomography, Park et al. (2007) found a -1.5% S-wave velocity anomaly at 200 km depth beneath the coast of the southern Red Sea, rising to ~-1% in the central Red Sea and to 0% or more in the northern Red Sea. A similar structure was found by Park et al. (2008) from Rayleigh wave tomography although with a more subdued northwards increase in S-wave velocity. They suggested this structure is caused by an upwelling of warm mantle beneath the southern Arabian shield, originating from the Afar hotspot. They proposed that this hot plume material flows from Afar underneath the southern and central Red Sea, and then extends northwards beneath Arabia, whereas the northern Red Sea (north of ~23°N) is without underlying hot mantle. Shear wave

splitting directions from Hansen et al. (2006) indicate that the hot mantle flow moves northwards rather than parallel to the Red Sea. This is supported by the azimuthal anisotropy analysis of Sebai et al. (2006). The upper mantle under the Red Sea is poorly resolved in such models as they are mainly based on teleseismic recordings along the coast of Saudi Arabia (no offshore recordings). Nevertheless, this general pattern of upper mantle structure is corroborated by $Na_{8.0}$ analyses of axial lavas (sodium oxide concentrations corrected for fractionation (Klein and Langmuir, 1987)), which indicate the upper mantle temperature in the Red Sea generally decreases by about 60°C from 18°N to 26°N (Haase et al., 2000).

More recently, Chang et al. (2011) have carried out an inversion of seismic travel times and waveforms that provides a more complete coverage of the area under the Red Sea. They found low velocity (hot) material is located beneath the southern Red Sea and Gulf of Aden, consistent with active seafloor spreading. They also suggested that the hot material at a depth of ~150 km does not extend north-westwards below the central and northern Red Sea areas, but forms a channel extending northward beneath Arabia. The comparative high velocities under the central Red Sea coincide with our data and, as we show later, this could be important for interpretation of our results.

3.0 Data and methods

3.1 Seismic reflection

The multi-channel seismic reflection survey was carried out by a geophysical services company in 1976 (Izzeldin, 1982). The data were collected using a Vaporchoc source with a streamer consisting of 48 channels 50 m apart for the deep-water survey (2.4 km streamer), and of 24 channels 50 m apart for the shallow-water survey (1.2 km streamer), positioned using a local radio navigation system. The data were processed (24-fold), with semblance analysis providing interval velocity every 3.6 km along-track, and moveout corrected. The locations of

seismic reflection profiles 7, 9, 11, 15, 17, 19, 21, 25, 27, 29, and 31 used in this study are shown in Figure 2.

Two-way travel times for the basement and seabed reflections were converted to depths below sea level (Figure 4) as follows. A P-wave velocity (V_p) of 1.538 km s^{-1} was used for the water according to the empirical equations of Mackenzie (1981), with typical Red Sea salinity of 40 ppt and temperature of 21°C. A 1.9 km/s V_p for the Plio-Pleistocene sediments was chosen based on the measurements of DSDP Leg 23 samples (Whitmarsh et al., 1974) and the results of seismic reflection and refraction surveys by Egloff et al. (1991) and Gaulier et al. (1988). A V_p of 4.21 km/s was used for the evaporites, based on seismic refraction data from Tramontini and Davies (1969), Girdler and Whitmarsh (1974), and Egloff et al. (1991).

3.2 Magnetic anomalies

3.2.1 Sources of magnetic data

Marine magnetic field measurements from towed magnetometers were obtained from the National Centers for Environmental Information (NCEI) (www.ngdc.noaa.gov/mgg). The data comprise residual magnetic anomalies after removal of the international geomagnetic reference field (IGRF) from the total field measurements. Figures 3a and 3c show the survey locations and contoured anomalies after further adjustments to correct IGRF errors of the individual surveys (see figure caption).

Major causes of magnetic anomalies are expected to be susceptibility and remanent magnetization variations within the basement produced by intrusive or extrusive volcanic bodies. To investigate possible magnetic sources, Werner deconvolution was applied to derive the magnetic source depths and apparent susceptibilities, which were calculated along individual segments of the magnetic lines (ungridded magnetic data) where they cross the

seismic reflection profiles of Izzeldin (1987) (Figure 3b), and then were projected to the seismic profiles.

3.2.2 Werner deconvolution

Werner deconvolution is an inverse method that is used to solve for magnetic source parameters (e.g., depth and susceptibility) from the observed magnetic field assuming that the sources comprise thin sheet-like bodies of semi-infinite extent (Werner, 1953). The total field from a thin sheet-like body is equal to the horizontal gradient of the total field caused by the edge of a thick body. Werner deconvolution exploits this idea to estimate likely parameters of dykes and other layered structures (Ku and Sharp, 1983). Although individual depth values derived using the method have large uncertainties and the method can produce some erroneous solutions, their depths have been shown generally to cluster within basement (Cochran and Karner, 2007; Karner et al., 1991).

The total magnetic anomaly caused by a dike or other tabular body is given as (Ku and Sharp, 1983):

$$T_{mag}(x,0)=\frac{A(x-x_0)+BD}{(x-x_0)^2+D^2} \quad (1)$$

where A=-2ΔT($J_x \sin I + J_z \cos I \sin\alpha$) , B=2ΔT(-$J_x \cos I \sin\alpha + J_z \sin I$) , x_0 is horizontal position of the top centre of the dike, D is depth to the top of the dike, $2\Delta T$ is thickness of the dike ($\Delta T << D$), $\boldsymbol{J_S}$=(J_x, J_z) is the vector sum of induced and remanent magnetization, I is magnetic inclination of the main field $\boldsymbol{F}$, and α is strike of the body measured counterclockwise from magnetic north.

Interference from neighbour anomalies or regional trends is incorporated in the form of a polynomial (Ku and Sharp, 1983):

240 $$T_{mag}(x,0)=\frac{A(x-x_0)+BD}{(x-x_0)^2+D^2}+C_0+C_1x+C_2x^2 \quad (2)$$

241 where $C_0+C_1x+C_2x^2$ are interference terms.

242 By rearranging equation (2), an inversion equation is obtained (Ku and Sharp, 1983; Rao,
243 1984):

244 $$a_0+a_1x+a_2x^2+a_3x^3+a_4x^4+b_0T_{mag}+b_1xT_{mag}=x^2T_{mag} \quad (3)$$

245 where

246
$$\begin{aligned}
a_0 &= -Ax_0+BD+C_0D^2+{x_0}^2C_0\\
a_1 &= A-2C_0x_0+C_1D^2+C_1{x_0}^2,\\
a_2 &= C_0-2C_1x_0+C_2D^2+C_2{x_0}^2,\\
a_3 &= C_1-2C_2x_0,\\
a_4 &= C_2,\\
b_0 &= -{x_0}^2-D^2,
\end{aligned}$$

247 and

248 $$b_1=2x_0$$

249 A seven-point Werner operator was applied to construct seven simultaneous equations for
250 inversion equation (3), with a sample spacing of Δx. Then, we obtain the following results for
251 the thin dike (Ku and Sharp, 1983):

252 Horizontal position: $X=0.5\,b_1\,\Delta x+x$ (4a)

253 Depth: $Y=\sqrt{-b_0-0.25\,b_1^2}\,\Delta x$ (4b)

254 Magnetic susceptibility: $\chi_m=\frac{\sqrt{{J_x}^2+{J_z}^2}}{|\boldsymbol{F}|}\Delta x$ (4c)

255 Marquardt's (1963) non-linear least-squares best-fit method was used to solve the
256 simultaneous equations, producing the estimates of magnetic source depth and susceptibility
257 shown in Figure 4.

258 Magnetic source depths were estimated from the magnetic anomalies where the sources lay
259 less than 5 km from the seismic lines. If the magnetic bodies recognized by Werner
260 deconvolution are real, the depth estimates should define either the upper boundaries of
261 dykes or the edges of other causative bodies, so magnetic source solutions tend to be tightly
262 grouped vertically beneath the true locations of the causative bodies (Cochran and Karner,
263 2007; Karner et al., 1991; Ku and Sharp, 1983). Therefore, the upper clusters of Werner
264 solutions were interpreted as the top of the magnetic basement.

265 3.3 Bathymetry data

266 We have used version 18.1 of the Smith and Sandwell (1997) bathymetry grid, which combines
267 shipboard depth measurements with depths inferred from satellite altimetry of the sea
268 surface. These data are shown in Figure 1. Comparisons of the bathymetry sampled along
269 the seismic lines with depths derived from the seabed reflection were used to verify the
270 positions of the seismic profiles.

271 3.4 Isostatic loading corrections

272 When assessing whether the geometry of crustal basement is typical of oceanic crust, it is
273 necessary to correct the observed basement depth for the effect of loading by the overlying
274 evaporites and sediment. We have used a simple 1-D Airy isostatic model (Airy, 1855; Watts,
275 2001) in which the isostatic depression, Δz, is:

276 $$\Delta z = \frac{(\rho_{es} - \rho_w)}{\rho_m - \rho_w} t_{es} \qquad (5)$$

where ρ_{es} is the mean density of the evaporite and sediment layers, ρ_m and ρ_w are the densities of mantle and seawater, and t_{es} is the total thickness of the evaporites and other sediments. A mean density of 2148 kg m^{-3} was used for the evaporite and sediment layers based on DSDP sample measurements of Wheildon et al. (1974). A density of 3220 kg m^{-3} was chosen for the hot mantle (Crough, 1983; Gvirtzman et al., 2016). A 1020 kg m^{-3} density was used for the seawater. Reversing isostatic depression, which was typically 1-2 km, produced the profiles shown in Figure 5a.

It was not possible to backstrip fully these sediments due to lack of detailed stratigraphic data, but industry well data show the evaporites were deposited from ~15 Ma, at the start of the Middle Miocene (Hughes and Beydoun, 1992) to ~5.3 Ma, at the end of the Miocene. This corresponds to times of active rifting, and continental rifts are typically weak, with a low effective elastic thickness (T_e) of 5-15 km (Watts and Burov, 2003). Young, slow-spreading oceanic lithosphere is also typically weak, with T_e < 13 km and commonly T_e < 5 km (Cochran, 1979; Kalnins, 2011). The assumption of Airy isostasy, ignoring lithospheric rigidity, will lead to overcorrected deep basement and undercorrected shallow basement compared with flexural isostasy (e.g., Watts, 2001); unloaded basement relief will thus also be underestimated. For the relatively weak Red Sea, this difference should be moderate. For a basin of comparable scale, Davison et al. (2012) estimated 0.5 km of isostatic overcorrection of their deepest basement for a T_e of 5 km.

To reveal the systematic trend of basement deepening with distance away from the axis, both western and eastern sides of the unloaded basement depth profiles were plotted together by offsetting each segment to their average axial depth of 1.69 km (Figure 5d). To help assess whether the crust is oceanic, we compare the observed subsidence with the global average oceanic crust subsidence curve (blue solid line in Figure 5d) from Crosby and McKenzie (2009) using the Chron 2A to present spreading rates of Chu and Gordon (1998). In doing so, we

assume that Red Sea opening prior to Chron 2A occurred with a similar opening pole and rate. Besides some offsets of dated features along the Dead Sea transform fault (e.g., Barjous and Mikbel, 1990; Garfunkel, 1981; Garfunkel et al., 1974) there are unfortunately no independent measures of Nubia-Arabia motion to confirm this unequivocally. However, other data from the Gulf of Aden at 14°N, 52°E show continuous spreading, with opening rate decreasing from ~30 mm year^{-1} at 15-17.5 Ma to ~20 mm year^{-1} at 10 Ma and then remaining constant to the present (Fournier et al., 2010).

3.5 Bouguer gravity anomalies

Gravity anomalies arise from density variations within the crust and upper mantle, as well as topography on the seabed, crust-evaporite, and Moho interfaces. Mitchell et al. (2017) computed marine Bouguer anomalies of the central Red Sea to remove the component of the gravity field due to the seabed topography.

We examine the correlation between the marine Bouguer anomalies and the basement depths for evidence of variations in crustal thickness or density or in mantle density. In regions of high correlation, we solve for the apparent density contrast ($\Delta\rho$) that best explains the observed gravity anomaly (Figure 7) to see if it is consistent with the expected density contrast between the mantle and the evaporites, assuming a constant thickness crust.

Apparent densities were derived from Bouguer-basement depth gradients $\frac{\partial g_B}{\partial h}$ by inverting the equation derived from the gravity slab formula:

$$-\frac{\partial g_B}{\partial h} = 2\pi G \Delta\rho \qquad (6)$$

where G is the universal constant of gravitation. The gradients $\frac{\partial g_B}{\partial h}$ were obtained by least-squares regression for data within 60 km of the axis (regions of high correlation). Using

equation (6) ignores effects of upward continuation; we explore these potential inaccuracies in section 4.3.

4.0 Results

4.1 Character of basement and seabed derived from seismic reflection profiles

In Figure 4, the seabed in all the seismic profiles forms an axial trough within ~20 km of the axis. The average depth of the axial trough shallows southwards from ~1.8 km in profile 7 to ~1.4 km in profile 29. The seismically derived seabed depths are generally consistent with Smith and Sandwell (1997, version 18.1) bathymetry, except in the axial trough of profile 9, where within 4 km of the axis, the seismically derived depth is 0.5 km shallower. Below the seabed, the S-reflection marking the top of the Miocene evaporites (Ross and Schlee, 1973) is found everywhere other than over the axial trough. The Plio-Pleistocene (PP) sediments overlying the S-reflection are thin (0.2-0.3 km thick) and tend to be uniform, as found in shallow seismic surveys (e.g., Phillips and Ross, 1970; Ross and Schlee, 1973).

The basement is considerably more rugged. The basement reflection is discontinuous, probably because of faulting, and in places completely absent or un-interpretable, a result of varied data quality. Basement outcrops directly on the seafloor in the axial trough and deepens progressively towards the coasts from an average depth of 1.69 km near the axis to ~6 km depth at a distance of ~60 km on both sides of the axial trough. Further landward, this trend changes: the basement rises steeply towards the coasts by up to 4 km in ~60 km distance, before becoming harder to identify in the seismic data near the coasts. On the western flank of profile 15, the reflection basement is not clear. Across the central Red Sea, the magnetic basement tops derived from Werner deconvolution are generally consistent with the seismic basement reflection depths. Additionally, only a minority of magnetic sources are found by the deconvolution within the evaporites or PP sediments.

348 *4.2 Oceanic-like axial crustal highs in isostatically corrected basement depths*

349 After correcting for evaporite and sediment loading, the data reveal axial highs in all profiles
350 (Figure 5a and 5d). They have plateaux 70-100 km wide with adjacent steep slopes deepening
351 by 0.8-1.6 km over a distance of 30-40 km (Figure 5a). Within the plateaux are axial troughs,
352 where basement typically outcrops over 14 km, forming a valley of varied size but on average
353 0.43 km deep (Figure 5d). Three profiles marked in green in Figure 5d differ from the others;
354 these lines lie furthest to the north and furthest from the Afar plume. The other basement
355 depth profiles have a broadly similar morphology. The basement deepens between ~35 km
356 from the axis (at the axial plateau edge) and ~60-100 km, with the average profile reaching a
357 minimum at ~80 km. Beyond there, the basement commonly ascends towards the coasts.
358 Axial crustal highs are not found in active magmatic rifts, which instead contain basement
359 depressions (Corti et al., 2004; Mohr, 1982; Rosendahl, 1987; Thybo and Nielsen, 2009).
360 However, an axial high is commonly found at spreading ridges located near mantle hotspots
361 where excess melting generates thicker and more elevated axial crust, such as the slow-
362 spreading Reykjanes Ridge near the Iceland hotspot (Searle and Laughton, 1981), the ultra-
363 slow spreading Spiess Ridge near the Bouvet hotspot (Mitchell and Livermore, 1998), and the
364 intermediate rate Galapagos Spreading Centre near the Galapagos hotspot (Blacic et al., 2008).

365 Based on the seismic profiles of Johansen et al. (1984), the Reykjanes Ridge axial crustal high
366 is ~40-60 km wide and rises 0.6-1.0 km above the surrounding topography (Figure 5b).
367 Although more pronounced than the Reykjanes Ridge, the Red Sea axial basement high may
368 imply that the central Red Sea has similarly experienced increased melt supply and enhanced
369 crustal thickness in the recent geological past. As shown in Figure 5a and 5b, the relief of the
370 Red Sea axial high does not vary systematically with distance from the Afar region, in contrast
371 with the axial relief of the Reykjanes Ridge, which increases systematically towards Iceland
372 (Jones et al., 2002; Vogt, 1971; White et al., 1995). Moreover, with a short-wavelength (<10

km) relief exceeding 150 m, the basement surface around the Red Sea axis is rougher than that near the Reykjanes Ridge.

4.3 Correlation between Bouguer gravity anomalies and basement reflection depths

There is a strong correlation between the Bouguer anomalies and the basement depths, although this correlation breaks down at distances greater than ~60 km from the ridge axis, where the basement shallows while the Bouguer anomaly stays subdued (Figure 6). This strong correlation suggests that the density interface between the evaporites and basement is a prominent contributor to the Bouguer anomaly, although other density contributions (crustal thickness, and mantle and crustal density) may also vary coherently with the deepening of basement. The changes near the coasts suggest a reduction in the average density of the materials within and beneath basement. This may reflect a change from oceanic crust around the axis to continental or transitional crust near the coasts.

If the mantle density and crustal thickness are both assumed for the sake of argument to be uniform, the correlation would be mainly due to the density contrast between mantle rocks and evaporites acting on the topography of the basement (a uniform crustal thickness would contribute a uniform amount to the gravity field, aside from upward continuation effects). The derived apparent density contrasts in Figure 7 vary from 220 to 580 kg m^{-3}, with no obvious trend with latitude. These contrasts are rather low compared with 1070 kg m^{-3} if hot mantle rocks of 3220 kg m^{-3} density (Crough, 1983; Gvirtzman et al., 2016) were contrasting with evaporite and other sediments of 2148 kg m^{-3} (Wheildon et al., 1974). The difference between the 1070 kg m^{-3} expected value and the 220-580 kg m^{-3} apparent density contrasts could arise from a combination of upward continuation effects, thickened crust, and hotter mantle beneath the axis.

396 The apparent density contrasts were computed based on the gravity slab formula, so it ignores
397 contributions to the gravity field arising from topographic changes on the basement and Moho
398 interfaces away from the points of observations. We carried out a simulation in which crust
399 with a uniform thickness of 7 km and uniform gabbroic density of 2900 kg m^{-3} (Hyndman and
400 Drury, 1977) overlies mantle with a uniform density of 3220 kg m^{-3} (Crough, 1983; Gvirtzman
401 et al., 2016). Figure 8 shows two simulations using basement relief from profile 21 (Figure 2).
402 To quantify the effect of upward continuation, theoretical Bouguer gravity anomalies (Figure
403 8c) computed from the models with and without the interface between basement and mantle
404 (Figures 8a and 8b) were used to derive graphs of Bouguer gravity anomaly versus basement
405 reflection depth and regression lines (Figure 8d) whose gradients were used to calculate
406 apparent density contrasts. Figure 8d shows that if only the topography on the evaporite-
407 basement interface were taken into account, the apparent density contrast between
408 evaporite and mantle would be 1006 kg m^{-3}. It also shows that if the topography on both
409 evaporite-basement interface and Moho were taken into account, the apparent density
410 contrast would be reduced by ~97 kg m^{-3} to 909 kg m^{-3}. We have also run the simulation with
411 varying basement depths, and found that upward continuation can reduce the apparent
412 density contrasts we infer using the gravity slab formula by up to ~160 kg m^{-3}.

413 Alternatively, the axial topography could reflect thickened crust. If the basement topography
414 is uncompensated, with a near-flat Moho, the gravity anomaly reflects the ~730 kg m^{-3} density
415 contrast between evaporite and oceanic crust, much closer to the values observed. This
416 further supports the view that the axial high is at least partly due to thickened crust. For a
417 model with 7 km of crust beneath the axis using Airy isostasy, so the topography on the Moho
418 compensates for the basement topography, our simulations suggest that an apparent density
419 contrast of ~575 kg m^{-3} would be observed. However, this is an extreme model, as it ignores
420 lateral variations in mantle density due to temperature variations.

421 Addressing those mantle temperature variations, upper mantle velocities varying from 7.4 to
422 7.8 km s^{-1} were reported for seismic refraction profile PIII of Egloff et al. (1991), which is
423 located in Figure 2. In Figure 9a, we show a density structure derived from their velocities
424 using density-velocity relations of Christensen and Shaw (1970). The model in Figure 9a is
425 generally isostatically balanced, though there are small imbalances at the oceanic-continental
426 boundary and around Suakin Deep (Figure 9c). The free-air anomalies predicted using 2D
427 gravity forward modelling successfully reproduce the observed free-air anomalies. It implies
428 a lateral mantle density variation of ~300 kg m^{-3} (Figure 9a). Using the basement topography
429 and Bouguer anomaly from 45 km to 85 km along profile PIII (outside the axial valley and east
430 of the ocean-continent transition), we derived an apparent density contrast of 880 kg m^{-3}.
431 The difference of 190 kg m^{-3} between 880 kg m^{-3} and 1070 kg m^{-3} could be due to mantle
432 density variation and upward continuation, since the line shows no variation in crustal
433 thickness, but does imply a variation in mantle density. More generally, we conclude that a
434 combination of crustal thickness variations, upward continuation, and mantle density
435 variations can potentially explain the low apparent density contrasts in Figure 7.

436 **5.0 Discussion**

437 As mentioned above, the axial highs with basement deepening with distance to 60 km from
438 the spreading axis (Figure 5) are more like those of oceanic crust than continental rifts, which
439 typically host depressions (Corti et al., 2004; Mohr, 1982; Rosendahl, 1987; Thybo and Nielsen,
440 2009). Prominent axial highs are common features of oceanic spreading ridges near mantle
441 hotspots (Blacic et al., 2008; Cochran and Sempéré, 1997; Hooft and Detrick, 1995; Searle and
442 Laughton, 1981). In the central Red Sea, the boundary of the oceanic crust to transitional or
443 continental crust likely occurs where the correlations between basement reflection depths
444 and Bouguer gravity anomalies break down, coinciding roughly with the transitions identified
445 by Izzeldin (1987). This boundary also coincides with a transition at ~60 km from the axis that

446 was interpreted by Egloff et al. (1991) from their velocity data near Suakin Deep (Figure 9).
447 We here compare the axial high to those of other spreading centres, examine its origin in more
448 detail and explore implications.

449 5.1 How does the Red Sea axial high compare with axial highs at other spreading centres near
450 hotspots?

451 Axial highs are usually associated with "magmatically robust" spreading centres, where the
452 crust is unusually thick (e.g., Blacic et al., 2008). For Reykjanes Ridge, it has been suggested
453 that the axial high is due to thickened crust resulting from enhanced mantle decompression
454 melting near to the Iceland hotspot (White et al., 1995). Using seismic reflection and
455 refraction data, Smallwood and White (1998) suggested that at ~62°N the Reykjanes Ridge
456 crust thins from 10 km on the ridge axis to 7.8 km on 5 Ma crust ~45 km from axis.

457 Figure 11 shows a compilation of bathymetry from other spreading centres near hotspots. It
458 includes an area south of the Azores, where a pair of ridges surrounding the Mid-Atlantic Ridge
459 (MAR) form a giant V-shape in plan-view, believed to have resulted from a pulse of magmatism
460 from the plume that has now ended, leaving the previous high rifted (Cannat et al., 1999;
461 Escartin et al., 2001). The Reykjanes Ridge is surrounded by more than one V-shaped ridge,
462 suggesting multiple pulses of magmatism (e.g., Parnell-Turner et al., 2017; Vogt, 1971). Ridges
463 surrounding the Galapagos Spreading Centre have been interpreted as arising from magmatic
464 pulses (Kappel and Ryan, 1986). Full spreading rates in these examples vary from ~16 mm yr^{-1}
465 to ~64 mm yr^{-1} (Chu and Gordon, 1998; DeMets et al., 1990; DeMets et al., 2010).

466 The axial relief in the central Red Sea (0.8-1.6 km) is similar to that at Spiess Ridge, more
467 pronounced than those at Reykjanes Ridge and Galapagos Spreading Centre, and lower than
468 those at the Mid-Atlantic Ridge near the Azores. The crustal thickness beneath the Spiess
469 Ridge was estimated to be ~11-15 km (Mitchell and Livermore, 1998), while the Galapagos

Spreading Centre axis near the Galápagos hotspot has a crustal thickness of only ~5.6-7.5 km (Canales et al., 2002).

Unlike the Reykjanes Ridge near Iceland and the Mid-Atlantic Ridge near the Azores, the central Red Sea axial high is not obviously surrounded by V-shaped ridges in either the gravity field (Figure 2) or from the seismic data (Figure 5a), suggesting that the influence of Afar hotspot on the opening of central Red Sea is not that strong. Whether this implies a lack of fluctuations in melt supply from the plume is unclear, as any such effect might be complicated by the fracture zones apparent from the cross-axis trends in the gravity field (Figure 2). Possible V-shaped ridges appear in the free-air gravity anomalies at 17˚-18˚N, closer to the Afar plume (Mitchell and Park, 2014).

5.2 How thick is crust beneath the axial high and how does it relate to mantle tomographic results?

In the central Red Sea, there is only one seismic refraction dataset capable of revealing crustal thickness (Egloff et al., 1991), and it did not reveal thickened crust under the spreading axis (Figure 9a). Alternative estimates of crustal thickness are available from geochemistry of the axial lavas. Sodium oxide concentrations in mid-ocean ridge basalt samples corrected for magma-chamber fractionation to 8% MgO ($Na_{8.0}$) have been interpreted by Klein and Langmuir (1987) as a measure of the depth-extent of mantle melting and shown to correlate with the thickness of oceanic crust derived from seismic refraction experiments. The $Na_{8.0}$ values from the Red Sea shown in Figure 10a (Haase et al., 2000; Ligi et al., 2012) increase systematically northwards implying decreasing crustal thickness, as expected from decreasing extents of melting and decreasing mantle temperature away from the Afar plume. We use the regression trend in Figure 10a to estimate the average $Na_{8.0}$ at the points where the seismic reflection lines cross the spreading axis. From the range of $Na_{8.0}$ and a regression of the Klein and Langmuir (1987) $Na_{8.0}$ data on crustal thickness, the central Red Sea axial crust

thickness is estimated to be ~5-10 km. This is similar to the mean of 7.1±0.8 km for normal oceanic crust (White et al., 1992), so the geochemical data do not indicate particularly thick crust. Furthermore, the basement is noticeably more rugged than the Reykjanes Ridge (Figure 5). This may be explained by a combination of (1) the slower spreading rate in the Red Sea, which leads to stronger, colder lithosphere closer to the ridge and larger abyssal hills (e.g., Malinverno, 1991; Sauter et al., 2011; Whittaker et al., 2008) and (2) potentially thinner crust in the Red Sea, which shows some correlation with greater roughness in slow to ultraslow spreading systems (Sauter et al., 2018).

To reconcile these observations, we speculate that the earliest seafloor spreading in the central Red Sea began with lower melt fluxes and thinner than average crust. Melt production then increased, increasing the crustal thickness to near average and creating the axial high. Based on current spreading rates of Chu and Gordon (1998) and the basement depths of Figure 5d, we suggest the axial high has developed since ~9 Ma. In Figure 5d, the basement is most elevated relative to the subsidence curve from 10 to 35 km off-axis, and returns to it by ~60 km. The rate of deepening from 10 to 35 km is too fast to be caused by normal thermal subsidence. If we interpret these variations in basement topography as solely due to thickened crust, the crust would be thickest 10 to 35 km from the axis and would thin to ~60 km, while the increasing elevation with distance within 10 km of the axis is most likely due to dynamic effects within the active rift (e.g., Buck et al., 2005; Schmalholz and Mancktelow, 2016; Tapponnier and Francheteau, 1978). This view of near normal crustal thickness is compatible with the recent mantle seismic velocity model of Chang et al. (2011), who showed low S-wave velocities associated with hotter mantle from the Afar plume extending beneath Arabia rather than beneath the central Red Sea (S-wave velocity beneath the southern Red Sea and Arabia is ~0.25 km s^{-1} lower than that beneath the central Red Sea). This extent of hot plume material could also explain why the influence of Afar hotspot on the opening of central Red Sea is not that strong (although the increased melt production could have been

affected by the Afar) and there is no relation to the distance from the Afar in the apparent density contrast (Figure 7).

In the Afar region, there have been pulses of volcanism (Audin et al., 2004; Barberi et al., 1975), so the variations in basement gradient in Figure 5d may have arisen from temporal changes in composition or temperature of the upwelling mantle. Others have remarked on the possibility of pulsating mantle plumes leaving V-shaped ridges south of Iceland and similar V-shaped ridges have been found elsewhere (e.g., Parnell-Turner et al., 2017; Vogt, 1971). However, no V-shaped ridges are observed in the central Red Sea; the crustal thickness variations appear to be consistent along the ridge.

Alternatively, a low initial melt supply may be a result of the mechanics of rifting mentioned in the introduction, if early melting was suppressed at the slow rifting rates due to conductive cooling or locally infertile mantle (Bonath, 1990; Zhou and Dick, 2013). Such a low melt supply would not be expected if there were enhanced mantle circulation at this stage as proposed by Buck (1986). We note that seaward thickening of oceanic crust is not always observed in seismic refraction datasets from other rifted margins (Peron-Pinvidic et al., 2013). However, seismic reflection and refraction data do show the crust thickens seaward at the oceanic–continental transition (OCT) on the Angolan margin (Contrucci et al., 2004; Moulin et al., 2005), indicating the South Atlantic Ocean basin there may have experienced an increase of melt production during early seafloor spreading as we suggest for the central Red Sea.

5.3 What are its implications?

If the axial high in the central Red Sea represents an increasingly thick crust but approaching only normal crustal thickness, the earlier spreading centre would have been deeper. The earlier evaporites may have therefore been deposited continuously across the ridge and not only on the flanks (as might otherwise have been the case in the south). This would in turn

imply that volcanic eruption occurred beneath or through the evaporites. Magma can heat adjacent evaporite and cause it to flow (Schofield et al., 2014). Augustin et al. (2016) proposed that the salt craters with raised rims found in the inter-trough zones were likely created by such eruptions, marking locations where volcanism continued after the area was covered by evaporites. Also, such eruptions ought to have geochemical consequences. For example, the evaporites affected could be rich in KCl and $CaCl_2$ but poor in $MgSO_4$ due to hydrothermal alteration of host basalts (e.g., Jackson et al., 2000), and sulfur isotope compositions of marine sulphates should be negatively shifted (e.g., Mills et al., 2017). Thus, if suitable samples could be recovered, the geochemistry of the evaporites could help to confirm the existence of a ridge buried by evaporites and map out its transition to exposed ridge.

6.0 Conclusions

To understand what type of crust underlies the central Red Sea, we carefully corrected for effects of overlying evaporite and other sediments to reconstruct basement geometry from 11 deep seismic reflection lines. The seismically derived basement depths corrected for evaporite and other sediment loading reveal an axial high typical of mid-ocean ridges affected by hotspots such as Reykjanes Ridge, where enhanced mantle melting results in thickened crust. In contrast, basement axial highs are not commonly observed at active amagmatic continental rifts. Its relief of ~1 km relative to a background subsidence trend is within the observed range. It is similar to that at Spiess Ridge, larger than that at Reykjanes Ridge, but smaller than that of the Mid-Atlantic Ridge near the Azores. We suggest the central Red Sea is underlain by oceanic crust and the central part of the Red Sea rift is an (ultra) slow spreading ridge influenced by the Afar hotspot, although our data do not reveal V-shaped ridges in this part of the Red Sea like those associated with plume pulses on the Reykjanes Ridge near Iceland or the Mid-Atlantic Ridge near the Azores.

569 Bouguer gravity anomalies calculated by correcting for the seabed topography are strongly
570 correlated with basement reflection depths with ~60 km of the axis. The apparent density
571 contrast implied by the correlation (220 to 580 kg m^{-3}) is too small for a uniform thickness
572 crust overlying a mantle of uniform density, which would lead to mantle rocks contrasting
573 with evaporites and a 1070 kg m^{-3} apparent density contrast. Around 160 kg m^{-3} of this
574 difference could be caused by an upward continuation effect (our method ignores topography
575 of interfaces). We suggest that the remaining discrepancy is caused by lower density mantle
576 and/or thicker crust towards the spreading axis, although variations in crustal density may
577 also contribute.

578 Geochemical data ($Na_{8.0}$) suggest that the crust has normal thickness beneath the present axis,
579 while the rugged basement topography is consistent with a slow to ultra-slow spreading ridge
580 with cold, rigid lithosphere and thin crust. To reconcile the axial high and gravity inversion
581 results, which suggest thickening crust towards the present day, with these other observations,
582 we speculate that the crust was unusually thin earlier in the evolution of the basin and has
583 recently thickened to a more normal thickness for a slow-spreading ridge.

584 **Acknowledgments**

585 We thank David Sandwell and Walter Smith for leading the gravity and bathymetry mapping
586 initiatives, and for the group involved in producing the grids used in our study. Figures were
587 prepared using the GMT software (Wessel et al., 2013). LMK is supported by a Royal Society
588 of Edinburgh Personal Research Fellowship funded by the Scottish Government. We also
589 thank Nico Augustin and an anonymous reviewer for helpful comments that significantly
590 improved the article.

591 **References**

592 Airy, G. B., 1855, On the computation of the effect of the attraction of mountain-masses, as
593 disturbing the apparent astronomical latitude of stations in geodetic surveys:
594 Philosophical Transactions of the Royal Society of London, v. 145, p. 101-104.
595 Almalki, K. A., P. G. Betts, and L. Ailleres, 2014, Episodic sea-floor spreading in the Southern
596 Red Sea: Tectonophysics, v. 617, p. 140-149.
597 Armitage, J. J., K. D. Petersen, and M. Pérez‐Gussinyé, 2018, The Role of Crustal Strength in
598 Controlling Magmatism and Melt Chemistry During Rifting and Breakup:
599 Geochemistry, Geophysics, Geosystems, v. 19, p. 534–550.
600 Atwater, T., and J. Stock, 1998, Pacific-North America plate tectonics of the Neogene
601 southwestern United States: an update: International Geology Review, v. 40, p. 375-
602 402.
603 Audin, L., X. Quidelleur, E. Coulié, V. Courtillot, S. Gilder, I. Manighetti, P. Y. Gillot, P.
604 Tapponnier, and T. Kidane, 2004, Palaeomagnetism and K‐Ar and 40Ar/39Ar ages in
605 the Ali Sabieh area (Republic of Djibouti and Ethiopia): constraints on the mechanism
606 of Aden ridge propagation into southeastern Afar during the last 10 Myr: Geophysical
607 Journal International, v. 158, p. 327-345.
608 Augustin, N., C. W. Devey, F. M. van der Zwan, P. Feldens, M. Tominaga, R. A. Bantan, and T.
609 Kwasnitschka, 2014, The rifting to spreading transition in the Red Sea: Earth and
610 Planetary Science Letters, v. 395, p. 217-230.
611 Augustin, N., F. M. van der Zwan, C. W. Devey, M. Ligi, T. Kwasnitschka, P. Feldens, R. A. Bantan,
612 and A. S. Basaham, 2016, Geomorphology of the central Red Sea Rift: Determining
613 spreading processes: Geomorphology, v. 274, p. 162-179.
614 Barberi, F., G. Ferrara, R. Santacroce, and J. Varet, 1975, Structural evolution of the Afar triple
615 junction: Afar depression of Ethiopia, v. 1, p. 38-54.
616 Barjous, M., and S. Mikbel, 1990, Tectonic evolution of the Gulf of Aqaba-Dead Sea transform
617 fault system: Tectonophysics, v. 180, p. 49-59.

618 Blacic, T. M., G. Ito, A. K. Shah, J. P. Canales, and J. Lin, 2008, Axial high topography and partial
619 melt in the crust and mantle beneath the western Galapagos Spreading Center:
620 Geochemistry, Geophysics, Geosystems, v. 9 (Paper Q12005,
621 doi:10.1029/2008GC002100).
622 Bonath, E., 1990, Not so hot" hot spots" in the oceanic mantle: Science, v. 250, p. 107-111.
623 Bonatti, E., 1985, Punctiform initiation of seafloor spreading in the Red Sea during transition
624 from a continental to an oceanic rift: Nature, v. 316, p. 33-37.
625 Bonatti, E., P. Hamlyn, and G. Ottonello, 1981, Upper mantle beneath a young oceanic rift:
626 peridotites from the island of Zabargad (Red Sea): Geology, v. 9, p. 474-479.
627 Bosworth, W., and K. McClay, 2001, Structural and stratigraphic evolution of the Gulf of Suez
628 rift, Egypt: a synthesis: Mémoires du Muséum national d'histoire naturelle, v. 186, p.
629 567-606.
630 Bosworth, W., M. Sultan, R. Stern, R. Arvidson, P. Shore, and R. Becker, 1993, Nature of the
631 Red Sea crust: A controversy revisited: Comment and Reply: Geology, v. 21, p. 574-
632 576.
633 Buck, W. R., 1986, Small-scale convection induced by passive rifting: the cause for uplift of rift
634 shoulders: Earth and Planetary Science Letters, v. 77, p. 362-372.
635 Buck, W. R., L. L. Lavier, and A. N. Poliakov, 2005, Modes of faulting at mid-ocean ridges:
636 Nature, v. 434, p. 719.
637 Canales, J. P., G. Ito, R. S. Detrick, and J. Sinton, 2002, Crustal thickness along the western
638 Galápagos Spreading Center and the compensation of the Galápagos hotspot swell:
639 Earth and Planetary Science Letters, v. 203, p. 311-327.
640 Cannat, M., A. Briais, C. Deplus, J. Escartín, J. Georgen, J. Lin, S. Mercouriev, C. Meyzen, M.
641 Muller, and G. Pouliquen, 1999, Mid-Atlantic Ridge–Azores hotspot interactions:
642 along-axis migration of a hotspot-derived event of enhanced magmatism 10 to 4 Ma
643 ago: Earth and Planetary Science Letters, v. 173, p. 257-269.

644 Carlson, R., 2001, The effects of temperature, pressure, and alteration on seismic properties
645 of diabase dike rocks from DSDP/ODP Hole 504B: Geophysical research letters, v. 28,
646 p. 3979-3982.
647 Carlson, R., 2010, How crack porosity and shape control seismic velocities in the upper oceanic
648 crust: Modeling downhole logs from Holes 504B and 1256D: Geochemistry,
649 Geophysics, Geosystems, v. 11 (Paper Q04007, doi:10.1029/2009GC002955).
650 Chang, S. J., M. Merino, S. Van der Lee, S. Stein, and C. A. Stein, 2011, Mantle flow beneath
651 Arabia offset from the opening Red Sea: Geophysical Research Letters, v. 38.
652 Christensen, N. I., and G. H. Shaw, 1970, Elasticity of mafic rocks from the Mid-Atlantic Ridge:
653 Geophysical Journal International, v. 20, p. 271-284.
654 Chu, D., and R. G. Gordon, 1998, Current plate motions across the Red Sea: Geophysical
655 Journal International, v. 135, p. 313-328.
656 Cochran, J., and G. Karner, 2007, Constraints on the deformation and rupturing of continental
657 lithosphere of the Red Sea: the transition from rifting to drifting: Geological Society,
658 London, Special Publications, v. 282, p. 265-289.
659 Cochran, J. R., 1979, An analysis of isostasy in the world's oceans: 2. Midocean ridge crests:
660 Journal of Geophysical Research: Solid Earth, v. 84, p. 4713-4729.
661 Cochran, J. R., 1983, A model for development of Red Sea: Aapg Bulletin, v. 67, p. 41-69.
662 Cochran, J. R., and F. Martinez, 1988, Evidence from the northern Red Sea on the transition
663 from continental to oceanic rifting: Tectonophysics, v. 153, p. 25-53.
664 Cochran, J. R., and J. C. Sempéré, 1997, The Southeast Indian Ridge between 88 E and 118 E:
665 Gravity anomalies and crustal accretion at intermediate spreading rates: Journal of
666 Geophysical Research: Solid Earth, v. 102, p. 15463-15487.
667 Contrucci, I., L. Matias, M. Moulin, L. Géli, F. Klingelhofer, H. Nouzé, D. Aslanian, J.-L. Olivet, J.-
668 P. Réhault, and J.-C. Sibuet, 2004, Deep structure of the West African continental

669 margin (Congo, Zaïre, Angola), between 5 S and 8 S, from reflection/refraction
670 seismics and gravity data: Geophysical Journal International, v. 158, p. 529-553.
671 Corti, G., M. Bonini, D. Sokoutis, F. Innocenti, P. Manetti, S. Cloetingh, and G. Mulugeta, 2004,
672 Continental rift architecture and patterns of magma migration: A dynamic analysis
673 based on centrifuge models: Tectonics, v. 23 (Paper TC2012,
674 doi:10.1029/2003TC001561).
675 Corti, G., J. Van Wijk, M. Bonini, D. Sokoutis, S. Cloetingh, F. Innocenti, and P. Manetti, 2003,
676 Transition from continental break‐up to punctiform seafloor spreading: How fast,
677 symmetric and magmatic: Geophysical Research Letters, v. 30 (Paper 1604, doi:
678 10.1029/2003GL017374).
679 Crosby, A., and D. McKenzie, 2009, An analysis of young ocean depth, gravity and global
680 residual topography: Geophysical Journal International, v. 178, p. 1198-1219.
681 Crough, S. T., 1983, The correction for sediment loading on the seafloor: Journal of
682 Geophysical Research: Solid Earth, v. 88, p. 6449-6454.
683 Davies, D., and C. Tramontini, 1970, The deep structure of the Red Sea: Philosophical
684 Transactions of the Royal Society of London A: Mathematical, Physical and
685 Engineering Sciences, v. 267, p. 181-189.
686 Davison, I., L. Anderson, and P. Nuttall, 2012, Salt deposition, loading and gravity drainage in
687 the Campos and Santos salt basins: Geological Society, London, Special Publications,
688 v. 363, p. 159-174.
689 DeMets, C., R. G. Gordon, D. Argus, and S. Stein, 1990, Current plate motions: Geophysical
690 journal international, v. 101, p. 425-478.
691 DeMets, C., R. G. Gordon, and D. F. Argus, 2010, Geologically current plate motions:
692 Geophysical Journal International, v. 181, p. 1-80.

693 Dyment, J., P. Tapponnier, A. Afifi, M. Zinger, D. Franken, and E. Muzaiyen, 2013, A New
694 Seafloor Spreading Model of the Red Sea: Magnetic Anomalies and Plate Kinematics:
695 AGU Fall Meeting Abstracts (T21A-2512).
696 Egloff, F., R. Rihm, J. Makris, Y. A. Izzeldin, M. Bobsien, K. Meier, P. Junge, T. Noman, and W.
697 Warsi, 1991, Contrasting Structural Styles Of the Eastern And Western Margins Of the
698 Southern Red-Sea - the 1988 Sonne Experiment: Tectonophysics, v. 198, p. 329-353.
699 Escartin, J., M. Cannat, G. Pouliquen, A. Rabain, and J. Lin, 2001, Crustal thickness of V‐
700 shaped ridges south of the Azores: Interaction of the Mid‐Atlantic Ridge (36–39 N)
701 and the Azores hot spot: Journal of Geophysical Research: Solid Earth, v. 106, p.
702 21719-21735.
703 Fletcher, R., N. Kusznir, and M. Cheadle, 2009, Melt initiation and mantle exhumation at the
704 Iberian rifted margin: Comparison of pure–shear and upwelling-divergent flow
705 models of continental breakup: Comptes Rendus Geoscience, v. 341, p. 394-405.
706 Fournier, M., N. Chamot‐Rooke, C. Petit, P. Huchon, A. Al‐Kathiri, L. Audin, M. O. Beslier, E.
707 d'Acremont, O. Fabbri, and J. M. Fleury, 2010, Arabia‐Somalia plate kinematics,
708 evolution of the Aden‐Owen‐Carlsberg triple junction, and opening of the Gulf of
709 Aden: Journal of Geophysical Research: Solid Earth, v. 115 (Paper B04102,
710 doi:10.1029/2008JB006257).
711 Furman, T., J. Bryce, T. Rooney, B. Hanan, G. Yirgu, and D. Ayalew, 2006, Heads and tails: 30
712 million years of the Afar plume: Geological Society, London, Special Publications, v.
713 259, p. 95-119.
714 Garfunkel, Z., 1981, Internal structure of the Dead Sea leaky transform (rift) in relation to plate
715 kinematics: Tectonophysics, v. 80, p. 81-108.
716 Garfunkel, Z., J. Bartov, Y. Eyal, and G. Steinitz, 1974, Raham Conglomerate–new evidence for
717 Neogene tectonism in the southern part of the Dead Sea Rift: Geological Magazine, v.
718 111, p. 55-64.

719 Gaulier, J., X. Le Pichon, N. Lyberis, F. Avedik, L. Geli, I. Moretti, A. Deschamps, and S. Hafez,
720 1988, Seismic study of the crust of the northern Red Sea and Gulf of Suez:
721 Tectonophysics, v. 153, p. 55-88.
722 Gaulier, J., X. Le Pichon, N. Lyberis, F. Avedik, L. Gely, and I. Moretti, 1986, New refraction data
723 on the Northern Red Sea-Gulf of Suez area: EOS Trans. Am. Geophys. Union, v. 67, p.
724 1208-1209.
725 George, R., N. Rogers, and S. Kelley, 1998, Earliest magmatism in Ethiopia: evidence for two
726 mantle plumes in one flood basalt province: Geology, v. 26, p. 923-926.
727 Gettings, M. E., H. Blank, W. Mooney, and J. Healey, 1986, Crustal structure of southwestern
728 Saudi Arabia: Journal of Geophysical Research: Solid Earth, v. 91, p. 6491-6512.
729 Girdler, R., and P. Styles, 1974, Two stage Red Sea floor spreading: Nature, v. 247, p. 7-11.
730 Girdler, R. W., and R. B. Whitmarsh, 1974, Miocene evaporites in Red Sea cores, their
731 relevance to the problem of the width and age of oceanic crust beneath the Red Sea:
732 in Whitmarsh, R.B., Weser, O.E., Ross, D.A.,et al., Initial Reports of the Deep Sea
733 Drilling Project, v. 23, p. 913-921.
734 Guennoc, P., G. Pautot, and A. Coutelle, 1988, Surficial structures of the northern Red Sea axial
735 valley from 23°N to 28°N : time and space evolution of neo-oceanic structures:
736 Tectonophysics, v. 153, p. 1-23.
737 Gvirtzman, Z., C. Faccenna, and T. W. Becker, 2016, Isostasy, flexure, and dynamic topography:
738 Tectonophysics, v. 683, p. 255-271.
739 Haase, K. M., R. Mühe, and P. Stoffers, 2000, Magmatism during extension of the lithosphere:
740 geochemical constraints from lavas of the Shaban Deep, northern Red Sea: Chemical
741 Geology, v. 166, p. 225-239.
742 Hall, S. A., 1989, Magnetic Evidence for the Nature Of the Crust beneath the Southern Red-
743 Sea: Journal Of Geophysical Research-Solid Earth And Planets, v. 94, p. 12267-12279.

744 Hansen, S., S. Schwartz, A. Al-Amri, and A. Rodgers, 2006, Combined plate motion and density-
745 driven flow in the asthenosphere beneath Saudi Arabia: Evidence from shear-wave
746 splitting and seismic anisotropy: Geology, v. 34, p. 869-872.
747 Harry, D., and J. Bowling, 1999, Inhibiting magmatism on nonvolcanic rifted margins: Geology,
748 v. 27, p. 895-898.
749 Hofmann, C., V. Courtillot, G. Feraud, P. Rochette, G. Yirgu, E. Ketefo, and R. Pik, 1997, Timing
750 of the Ethiopian flood basalt event and implications for plume birth and global change:
751 Nature, v. 389, p. 838-841.
752 Hooft, E. E., and R. S. Detrick, 1995, Relationship between axial morphology, crustal thickness,
753 and mantle temperature along the Juan de Fuca and Gorda Ridges: Journal of
754 Geophysical Research: Solid Earth, v. 100, p. 22499-22508.
755 Hopper, J. R., and W. Roger Buck, 1998, Styles of extensional decoupling: Geology, v. 26, p.
756 699-702.
757 Hughes, G., and Z. Beydoun, 1992, The Red Sea—Gulf of Aden: biostratigraphy,
758 lithostratigraphy and palaeoenvironments: Journal of Petroleum Geology, v. 15, p.
759 135-156.
760 Hyndman, R., and M. Drury, 1977, Physical properties of basalts, gabbros, and ultramafic rocks
761 from DSDP Leg 37: DSDP, v. 37, p. 395-401.
762 Izzeldin, A., 1982, On the structure and evolution of the Red Sea: Diss. Univ. Strasbourg.
763 Izzeldin, A., 1987, Seismic, gravity and magnetic surveys in the central part of the Red Sea:
764 their interpretation and implications for the structure and evolution of the Red Sea:
765 Tectonophysics, v. 143, p. 269-306.
766 Izzeldin, A., 1989, Transverse structures in the central part of the Red Sea and implications on
767 early stages of oceanic accretion: Geophysical Journal International, v. 96, p. 117-129.

768 Jackson, M. P., C. Cramez, and J.-M. Fonck, 2000, Role of subaerial volcanic rocks and mantle
769 plumes in creation of South Atlantic margins: implications for salt tectonics and source
770 rocks: Marine and Petroleum Geology, v. 17, p. 477-498.
771 Jeanniot, L., N. Kusznir, G. Mohn, G. Manatschal, and L. Cowie, 2016, Constraining lithosphere
772 deformation modes during continental breakup for the Iberia–Newfoundland
773 conjugate rifted margins: Tectonophysics, v. 680, p. 28-49.
774 Johansen, B., P. R. Vogt, and O. Eldholm, 1984, Reykjanes Ridge: further analysis of crustal
775 subsidence and time-transgressive basement topography: Earth and planetary
776 science letters, v. 68, p. 249-258.
777 Jones, S. M., N. White, and J. Maclennan, 2002, V‐shaped ridges around Iceland: Implications
778 for spatial and temporal patterns of mantle convection: Geochemistry, Geophysics,
779 Geosystems, v. 3 (Paper 1059, doi:10.1029/2002GC000361).
780 Kalnins, L. M., 2011, Spatial variations in the effective elastic thickness of the lithosphere and
781 their tectonic implications, Oxford University, 251-325 p.
782 Kappel, E. S., and W. B. Ryan, 1986, Volcanic episodicity and a non‐steady state rift valley
783 along northeast Pacific spreading centers: Evidence from Sea MARC I: Journal of
784 Geophysical Research: Solid Earth, v. 91, p. 13925-13940.
785 Karbe, L., 1987, Hot brines and the deep sea environment, AJ Edwards, and SM Head (Oxford:
786 Pergamon Press).
787 Karner, G., N. Driscoll, and J. Peirce, 1991, Gravity and magnetic signature of broken ridge,
788 southeast Indian Ocean: Proceedings of the Ocean Drilling Program, Scientific Results,
789 p. 681-695.
790 Klein, E. M., and C. H. Langmuir, 1987, Global correlations of ocean ridge basalt chemistry with
791 axial depth and crustal thickness: Journal of Geophysical Research: Solid Earth, v. 92,
792 p. 8089-8115.

793 Ku, C. C., and J. A. Sharp, 1983, Werner deconvolution for automated magnetic interpretation
794 and its refinement using Marquardt's inverse modeling: Geophysics, v. 48, p. 754-774.
795 LaBrecque, J., and N. Zitellini, 1985, Continuous sea-floor spreading in Red Sea: an alternative
796 interpretation of magnetic anomaly pattern: AAPG Bulletin, v. 69, p. 513-524.
797 Levi, S., and R. Riddihough, 1986, Why are marine magnetic anomalies suppressed over
798 sedimented spreading centers?: Geology, v. 14, p. 651-654.
799 Ligi, M., E. Bonatti, G. Bortoluzzi, A. Cipriani, L. Cocchi, F. Caratori Tontini, E. Carminati, L.
800 Ottolini, and A. Schettino, 2012, Birth of an ocean in the Red Sea: initial pangs:
801 Geochemistry, Geophysics, Geosystems, v. 13 (Paper Q08009,
802 doi:10.1029/2012GC004155).
803 Ligi, M., E. Bonatti, W. Bosworth, Y. Cai, A. Cipriani, C. Palmiotto, S. Ronca, and M. Seyler, 2018,
804 Birth of an ocean in the Red Sea: Oceanic-type basaltic melt intrusions precede
805 continental rupture: Gondwana Research, v. 54, p. 150-160.
806 Ligi, M., E. Bonatti, F. C. Tontini, A. Cipriani, L. Cocchi, A. Schettino, G. Bortoluzzi, V. Ferrante,
807 S. Khalil, and N. C. Mitchell, 2011, Initial burst of oceanic crust accretion in the Red
808 Sea due to edge-driven mantle convection: Geology, v. 39, p. 1019-1022.
809 Lonsdale, P., 1989, Geology and tectonic history of the Gulf of California: The eastern Pacific
810 Ocean and Hawaii: Boulder, Colorado, Geological Society of America, Geology of
811 North America, v. N, p. 499-521.
812 Mackenzie, K. V., 1981, Discussion of sea water sound‐speed determinations: The Journal of
813 the Acoustical Society of America, v. 70, p. 801-806.
814 Malinverno, A., 1991, Inverse square-root dependence of mid-ocean-ridge flank roughness on
815 spreading rate: Nature, v. 352, p. 58-60.
816 Marquardt, D. W., 1963, An algorithm for least-squares estimation of nonlinear parameters:
817 Journal of the society for Industrial and Applied Mathematics, v. 11, p. 431-441.

818 Martinez, F., and J. R. Cochran, 1988, Structure and tectonics of the northern Red Sea: catching
819 a continental margin between rifting and drifting: Tectonophysics, v. 150, p. 1-31.
820 Martinez, F., B. Taylor, and A. M. Goodliffe, 1999, Contrasting styles of seafloor spreading in
821 the Woodlark Basin: Indications of rift ‐ induced secondary mantle convection:
822 Journal of Geophysical Research: Solid Earth, v. 104, p. 12909-12926.
823 Marty, J. C., and A. Cazenave, 1989, Regional variations in subsidence rate of oceanic plates:
824 a global analysis: Earth and Planetary Science Letters, v. 94, p. 301-315.
825 McKenzie, D., D. Davies, and P. Molnar, 1970, Plate tectonics of the Red Sea and east Africa:
826 Nature, v. 226, p. 243.
827 Meyer, B., R. Saltus, and A. Chulliat, 2017, EMAG2: Earth magnetic anomaly grid (2-arc-minute
828 resolution) version 3: National Centers for Environmental Information, NOAA. Model.
829 doi, v. 10, p. V5H70CVX.
830 Mills, J. V., M. L. Gomes, B. Kristall, B. B. Sageman, A. D. Jacobson, and M. T. Hurtgen, 2017,
831 Massive volcanism, evaporite deposition, and the chemical evolution of the Early
832 Cretaceous ocean: Geology, v. 45, p. 475-478.
833 Mitchell, N. C., M. Ligi, P. Feldens, and C. Hübscher, 2017, Deformation of a young salt giant:
834 regional topography of the Red Sea Miocene evaporites: Basin Research, v. 29, p. 352-
835 369.
836 Mitchell, N. C., and R. A. Livermore, 1998, Spiess Ridge: An axial high on the slow spreading
837 Southwest Indian Ridge: Journal of Geophysical Research: Solid Earth, v. 103, p.
838 15457-15471.
839 Mitchell, N. C., and Y. Park, 2014, Nature of crust in the central Red Sea: Tectonophysics, v.
840 628, p. 123-139.
841 Mohr, P., 1982, Musings on continental rifts: In: Palmason, G. (Ed.), Continental and oceanic
842 rifts. American Geophysical Union, Geodynamic Series, v. 8, p. 293-309.
843 Mohr, P., 1983, Ethiopian flood basalt province: Nature, v. 303, p. 577-584.

844 Mooney, W. D., M. E. Gettings, H. R. Blank, and J. H. Healy, 1985, Saudi Arabian seismic-
845 refraction profile: a traveltime interpretation of crustal and upper mantle structure:
846 Tectonophysics, v. 111, p. 173-246.
847 Moulin, M., D. Aslanian, J.-L. Olivet, I. Contrucci, L. Matias, L. Géli, F. Klingelhoefer, H. Nouzé,
848 J.-P. Réhault, and P. Unternehr, 2005, Geological constraints on the evolution of the
849 Angolan margin based on reflection and refraction seismic data (ZaïAngo project):
850 Geophysical Journal International, v. 162, p. 793-810.
851 Omar, G. I., and M. S. Steckler, 1995, Fission track evidence on the initial rifting of the Red Sea:
852 two pulses, no propagation: Science, v. 270, p. 1341-1344.
853 Park, Y., A. A. Nyblade, A. J. Rodgers, and A. Al‐Amri, 2007, Upper mantle structure beneath
854 the Arabian Peninsula and northern Red Sea from teleseismic body wave tomography:
855 Implications for the origin of Cenozoic uplift and volcanism in the Arabian Shield:
856 Geochemistry, Geophysics, Geosystems, v. 8 (Paper Q06021,
857 doi:10.1029/2006GC001566).
858 Park, Y., A. A. Nyblade, A. J. Rodgers, and A. Al‐Amri, 2008, S wave velocity structure of the
859 Arabian Shield upper mantle from Rayleigh wave tomography: Geochemistry,
860 Geophysics, Geosystems, v. 9 (Paper Q07020, doi:10.1029/2007GC001895).
861 Parnell‐Turner, R., N. White, T. J. Henstock, S. M. Jones, J. Maclennan, and B. J. Murton, 2017,
862 Causes and Consequences of Diachronous V‐Shaped Ridges in the North Atlantic
863 Ocean: Journal of Geophysical Research: Solid Earth, v. 122, p. 8675–8708.
864 Peron-Pinvidic, G., G. Manatschal, and P. T. Osmundsen, 2013, Structural comparison of
865 archetypal Atlantic rifted margins: A review of observations and concepts: Marine and
866 Petroleum Geology, v. 43, p. 21-47.
867 Pautot, G., P. Guennoc, A. Coutelle, and N. Lyberis, 1984, Discovery of a large brine deep in
868 the northern Red Sea: Nature, v. 310, p. 133.

869 Phillips, J. D., 1970, Magnetic anomalies in the Red Sea: Philosophical Transactions of the Royal
870 Society of London A: Mathematical, Physical and Engineering Sciences, v. 267, p. 205-
871 217.
872 Phillips, J. D., and D. A. Ross, 1970, Continuous seismic reflexion profiles in the Red Sea:
873 Philosophical Transactions of the Royal Society of London A: Mathematical, Physical
874 and Engineering Sciences, v. 267, p. 143-152.
875 Rao, V. B., 1984, On:"Werner deconvolution for automated magnetic interpretation and its
876 refinement using Marquardt's inverse modeling" by CC Ku and JA Sharp (Geophysics,
877 v 48, p. 754–774, June, 1983): Geophysics, v. 49, p. 1119-1119.
878 Rasul, N. M., I. C. Stewart, and Z. A. Nawab, 2015, Introduction to the Red Sea: Its Origin,
879 Structure, and Environment, The Red Sea, Springer, p. 1-28.
880 Richards, M. A., R. A. Duncan, and V. E. Courtillot, 1989, Flood basalts and hot-spot tracks:
881 plume heads and tails: Science, v. 246, p. 103-107.
882 Rihm, R., and C. Henke, 1998, Geophysical studies on early tectonic controls on Red Sea rifting,
883 opening and segmentation, Sedimentation and Tectonics in Rift Basins Red Sea – Gulf
884 of Aden, Springer, p. 29-49.Ros, E., M. Pérez‐Gussinyé, M. Araújo, M. Thoaldo
885 Romeiro, M. Andrés‐Martínez, and J. P. Morgan, 2017, Lower Crustal Strength
886 Controls on Melting and Serpentinization at Magma‐Poor Margins: Potential
887 Implications for the South Atlantic: Geochemistry, Geophysics, Geosystems, v. 18, p.
888 4538–4557.
889 Rosendahl, B. R., 1987, Architecture of continental rifts with special reference to East Africa:
890 Annual Review of Earth and Planetary Sciences, v. 15, p. 445-503.
891 Ross, D. A., and J. Schlee, 1973, Shallow structure and geologic development of the southern
892 Red Sea: Geological Society of America Bulletin, v. 84, p. 3827-3848.

893 Sandwell, D. T., R. D. Muller, W. H. F. Smith, E. Garcia, and R. Francis, 2014, New global marine
894 gravity model from CryoSat-2 and Jason-1 reveals buried tectonic structure: Science,
895 v. 346, p. 65-67.
896 Sandwell, D. T., and W. H. Smith, 2009, Global marine gravity from retracked Geosat and ERS ‐
897 1 altimetry: Ridge segmentation versus spreading rate: Journal of Geophysical
898 Research: Solid Earth (1978–2012), v. 114.Sauter, D., H. Sloan, M. Cannat, J. Goff, P.
899 Patriat, M. Schaming, and W. R. Roest, 2011, From slow to ultra-slow: How does
900 spreading rate affect seafloor roughness and crustal thickness?: Geology, v. 39, p. 911-
901 914.
902 Sauter, D., J. Tugend, M. Gillard, M. Nirrengarten, J. Autin, G. Manatschal, M. Cannat, S. Leroy,
903 and M. Schaming, 2018, Oceanic basement roughness alongside magma-poor rifted
904 margins: insight into initial seafloor spreading: Geophysical Journal International, v.
905 212, p. 900-915.
906 Schmalholz, S. M., and N. S. Mancktelow, 2016, Folding and necking across the scales: a review
907 of theoretical and experimental results and their applications: Solid Earth, v. 7, p.
908 1417-1465.
909 Schofield, N., I. Alsop, J. Warren, J. R. Underhill, R. Lehné, W. Beer, and V. Lukas, 2014,
910 Mobilizing salt: Magma-salt interactions: Geology, v. 42, p. 599-602.
911 Schouten, H., H. J. Dick, and K. D. Klitgord, 1987, Migration of mid-ocean-ridge volcanic
912 segments: Nature, v. 326, p. 835-839.
913 Searle, R., and A. Laughton, 1981, Fine-scale sonar study of tectonics and volcanism on the
914 Reykjanes Ridge: Oceanologica Acta, v. 4, p. 5-13.
915 Sebai, A., E. Stutzmann, J.-P. Montagner, D. Sicilia, and E. Beucler, 2006, Anisotropic structure
916 of the African upper mantle from Rayleigh and Love wave tomography: Physics of the
917 Earth and Planetary Interiors, v. 155, p. 48-62.

Sempéré, J.-C., G. Purdy, and H. Schouten, 1990, Segmentation of the Mid-Atlantic Ridge between 24 N and 30 40'N.

Shi, W., N. Mitchell, and L. Kalnins, 2017, Assessing the nature of crust in the central Red Sea using potential field methods: EGU General Assembly Conference Abstracts, p. 542.

Smallwood, J. R., and R. S. White, 1998, Crustal accretion at the Reykjanes Ridge, 61–62 N: Journal of Geophysical Research: Solid Earth (1978–2012), v. 103, p. 5185-5201.

Smith, W. H. F., and D. T. Sandwell, 1997, Global Sea Floor Topography from Satellite Altimetry and Ship Depth Soundings: Science, v. 277, p. 1956-1962.

Sultan, M., R. Becker, R. E. Arvidson, P. Shore, R. J. Stern, Z. Elalfy, and E. A. Guinness, 1992, Nature of the Red Sea crust: A controversy revisited: Geology, v. 20, p. 593-596.

Tapponnier, P., J. Dyment, M. Zinger, D. Franken, A. Afifi, A. Wyllie, H. Ali, and I. Hanbal, 2013, Revisiting Seafloor-Spreading in the Red Sea: Basement Nature, Transforms and Ocean-Continent Boundary: AGU Fall Meeting Abstracts (T12B-04).

Tapponnier, P., and J. Francheteau, 1978, Necking of the lithosphere and the mechanics of slowly accreting plate boundaries: Journal of Geophysical Research: Solid Earth (1978–2012), v. 83, p. 3955-3970.

Thybo, H., and C. A. Nielsen, 2009, Magma-compensated crustal thinning in continental rift zones: Nature, v. 457, p. 873-876.

Tramontini, C., and D. Davies, 1969, A Seismic Refraction Survey in The Red Sea: Geophysical Journal International, v. 17, p. 225-241.

Vine, F. J., 1966, Spreading of the ocean floor: new evidence: Science, v. 154, p. 1405-1415.

Vogt, P., 1971, Asthenosphere motion recorded by the ocean floor south of Iceland: Earth and Planetary Science Letters, v. 13, p. 153-160.

Watts, A., and E. Burov, 2003, Lithospheric strength and its relationship to the elastic and seismogenic layer thickness: Earth and Planetary Science Letters, v. 213, p. 113-131.

943 Watts, A. B., 2001, Isostasy and Flexure of the Lithosphere: UK, Cambridge University Press,
944 1-284 p.
945 Weissel, J. K., B. Taylor, and G. D. Karner, 1982, The opening of the Woodlark Basin, subduction
946 of the Woodlark spreading system, and the evolution of northern Melanesia since
947 mid-Pliocene time: Tectonophysics, v. 87, p. 253-277.
948 Werner, S., 1953, Interpretation of magnetic anomalies at sheet-like bodies: Sveriges Geol:
949 Undersok. Ser. C. Arsbok, v. 43, p. 1949.
950 Wessel, P., W. H. Smith, R. Scharroo, J. Luis, and F. Wobbe, 2013, Generic mapping tools:
951 improved version released: Eos, Transactions American Geophysical Union, v. 94, p.
952 409-410.
953 Wheildon, J., T. Evans, R. Girdler, R. Whitmarch, O. Weser, and D. Ross, 1974, Thermal
954 conductivity, density, and sonic velocity measurements of samples of anhydrite and
955 halite from Sites 225 and 227: Initial Reports of the Deep Sea Drilling Project, v. 23, p.
956 909-911.
957 White, R., J. Bown, and J. Smallwood, 1995, The temperature of the Iceland plume and origin
958 of outward-propagating V-shaped ridges: Journal of the Geological Society, v. 152, p.
959 1039-1045.
960 White, R. S., D. McKenzie, and R. K. O'Nions, 1992, Oceanic crustal thickness from seismic
961 measurements and rare earth element inversions: Journal of Geophysical Research:
962 Solid Earth, v. 97, p. 19683-19715.
963 Whitmarsh, R., O. Weser, and D. Ross, 1974, Initial reports of the deep sea drilling project: US
964 Government Printing Office, Washington, v. 23b.
965 Whittaker, J. M., R. D. Müller, W. R. Roest, P. Wessel, and W. H. Smith, 2008, How
966 supercontinents and superoceans affect seafloor roughness: Nature, v. 456, p. 938-
967 941.

968 Withjack, M. O., and W. R. Jamison, 1986, Deformation produced by oblique rifting:
969 Tectonophysics, v. 126, p. 99-124.

970 Zhou, H., and H. J. Dick, 2013, Thin crust as evidence for depleted mantle supporting the
971 Marion Rise: Nature, v. 494, p. 195.

972

973 **Figure captions**

974

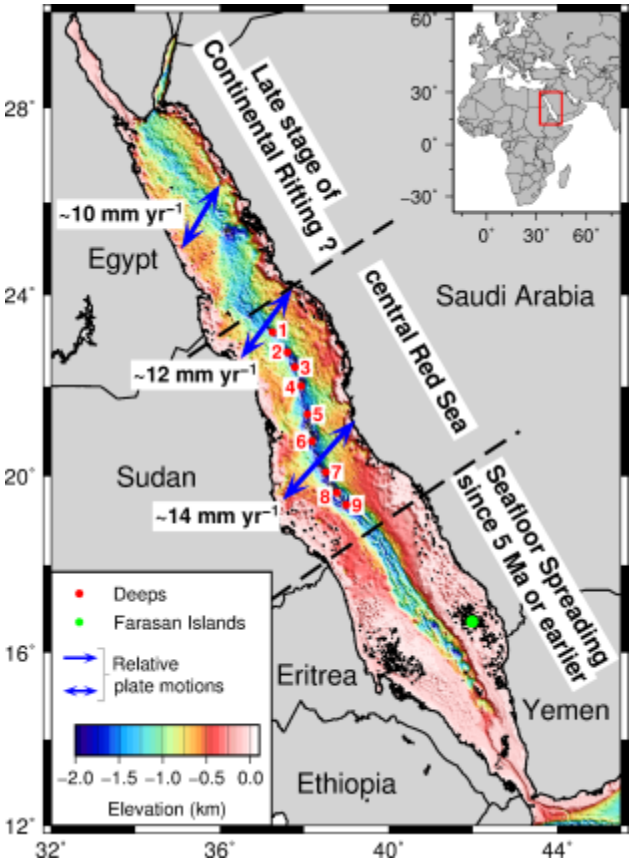

975

976 **Figure 1** Bathymetry of the Red Sea (Smith and Sandwell, 1997, version 18.1). Red dots locate
977 the prominent deeps in the central Red Sea from Augustin et al. (2014) and Karbe (1987).
978 From north to south, these are (1) Nereus, (2) Thetis, (3) Hadarba, (4) Hatiba, (5) Atlantis II, (6)
979 Erba, (7) Port Sudan, (8) Suakin, and (9) Pelagia deeps. Green dot marks the Farasan Islands.
980 The relative plate motion vectors were predicted using the Chu and Gordon (1998) plate
981 rotation pole.

982

983

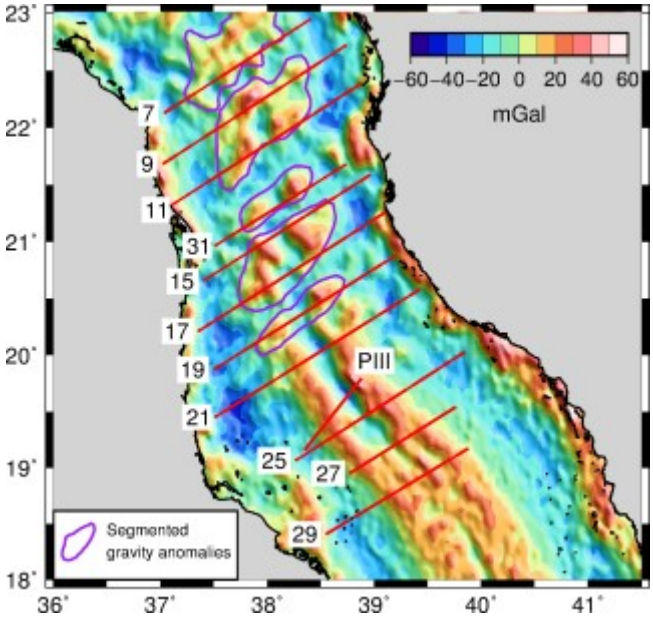

984

985 **Figure 2** Free-air gravity anomalies (Sandwell et al., 2014, version 23.1) and locations of

986 multichannel seismic reflection profiles 7, 9, 11, 15, 17, 19, 21, 25, 27, 29, 31 of Izzeldin

987 (1987) and seismic refraction profile SO53-PIII of Egloff et al. (1991). Purple curves show the

988 segmentation of gravity anomalies in the centre of the basin.

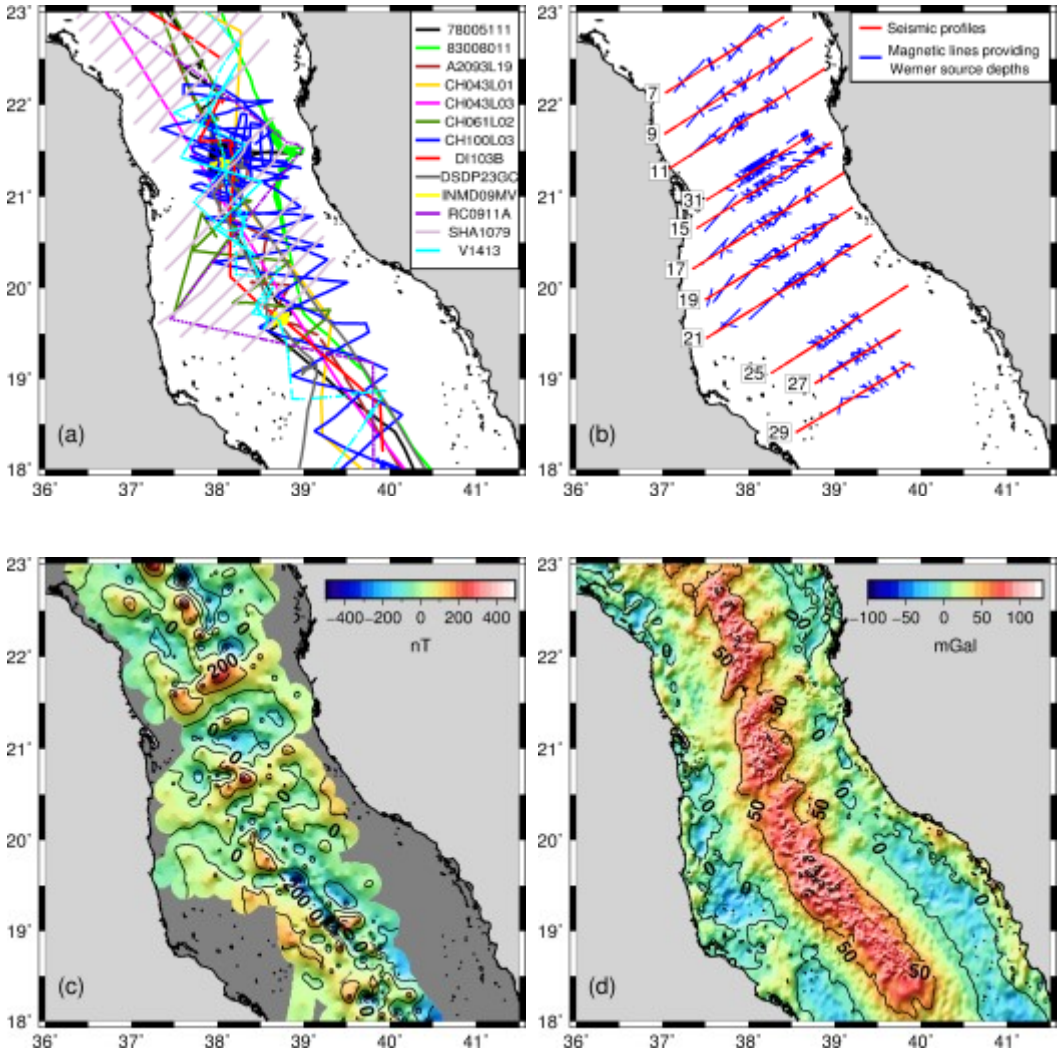

Figure 3 (a): Tracks of shipboard magnetic surveys of RVs *Jean Charcot* (78005111, 83008011), *Atlantis* (A2093L19), *Chain* (CH043L01, CH043L03, CH061L02, CH100L03), *Discovery* (DI103B), *Glomar Challenger* (DSDP23GC), *Melville* (INMD09MV), *Robert Conrad* (RC0911A), *Shackleton* (SHA1079) and *Vema* (V1413). (b): Extents of magnetic lines (blue) contributing to the seismic profiles (red) of Werner source depths. (c): Residual magnetic anomalies of the surveys in (a) obtained from the National Centers for Environmental Information (NCEI) (www.ngdc.noaa.gov/mgg) gridded and contoured every 50 nT. To reduce effects of reference field errors, the residual anomalies of each survey were adjusted by subtracting their mean value before gridding and contouring. (Anomalies are not reduced to the pole.) (d):

1001 Bouguer gravity anomalies from Mitchell et al. (2017) computed by removing the component
1002 of the free-air gravity field (Sandwell et al., 2014, version 23.1) due to the seabed topography.

1003

1004

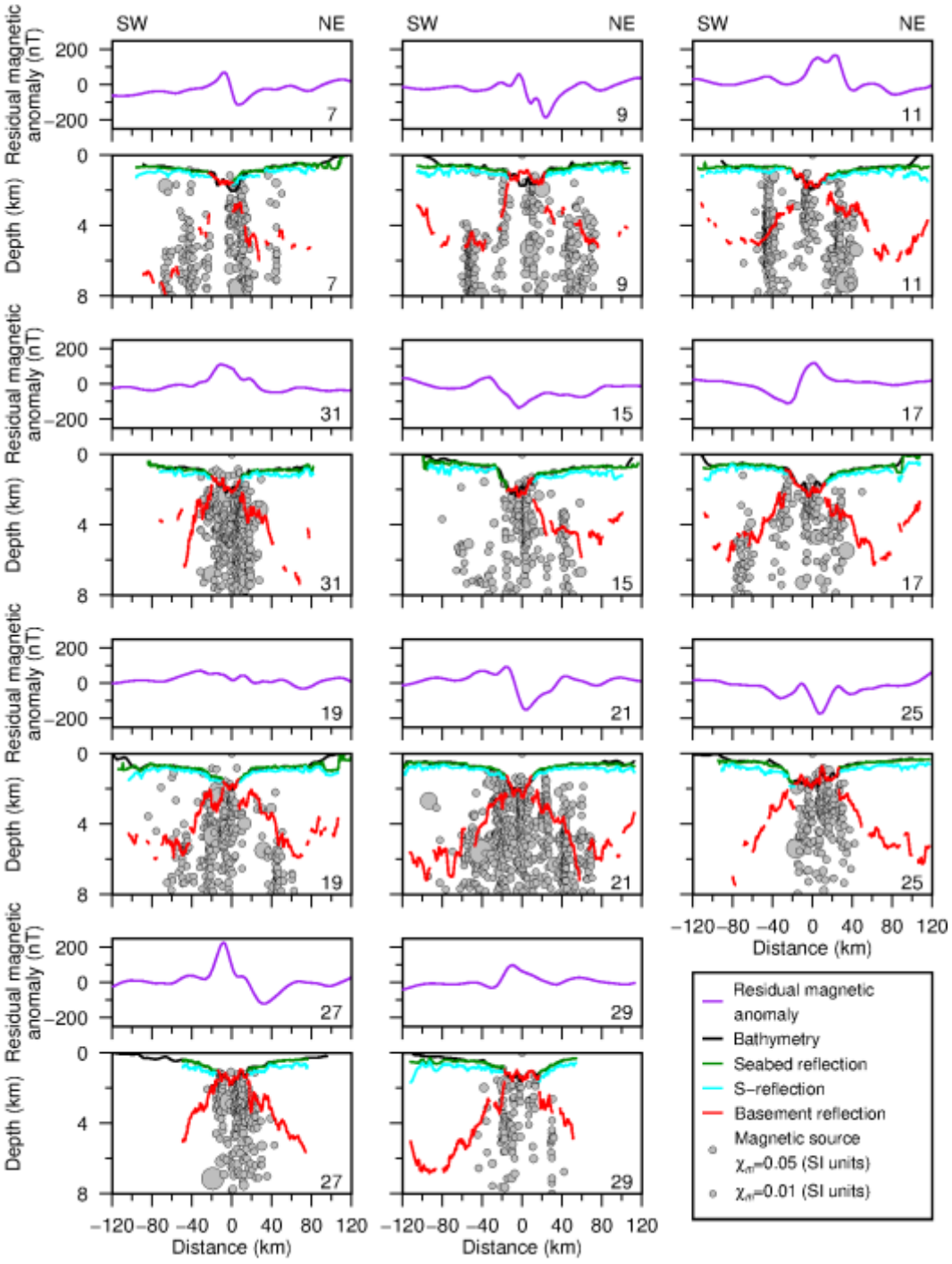

1005

1006 **Figure 4** Depths derived from the seismic reflection profiles of Izzeldin (1987) and Werner
1007 deconvolution of marine magnetic data. Line numbers are shown in the lower right corner of
1008 each panel. Magnetic anomalies (purple lines) along the seismic profiles were sampled from
1009 the EMAG2 v3 grid (Meyer et al., 2017). Black lines denote bathymetry (Smith and Sandwell,

1997, version 18.1). Dark green, cyan, and red lines are the depths of the seabed, the S-reflection at the top of the Miocene evaporites, and the basement, respectively, derived from the seismic reflection data. Grey circles are Werner source depth solutions, with circle size proportional to $log_2(\chi_m + 2)$. Depth estimates tend to cluster vertically beneath the true location of the causative body, with magnetic basement being interpreted around the top of the vertical clusters of solution depths. The Werner solutions generally confirm the seismically derived basement depths.

1018

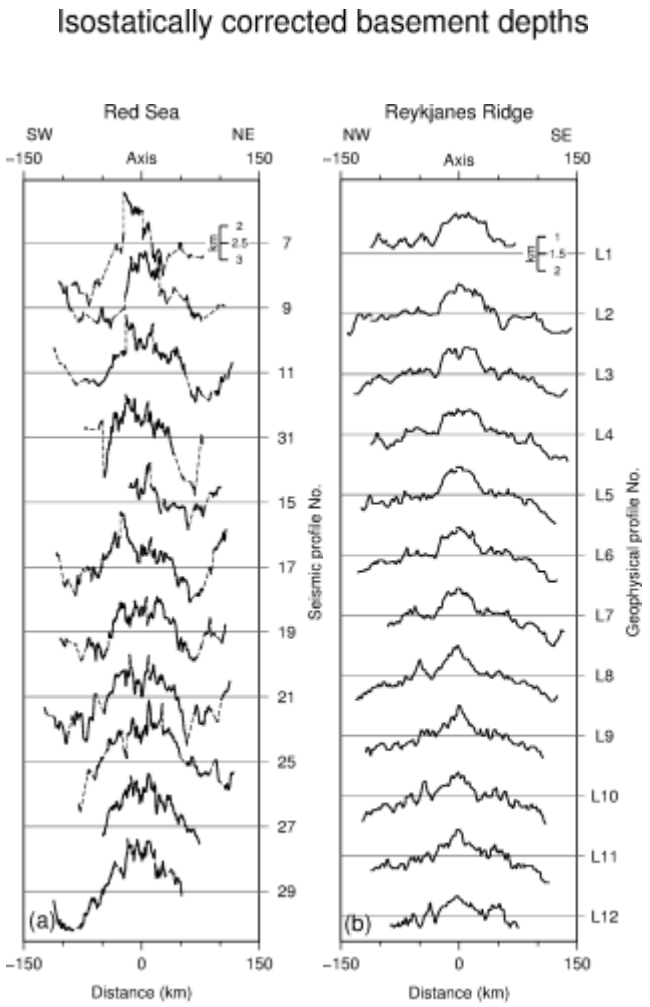

1019

1020

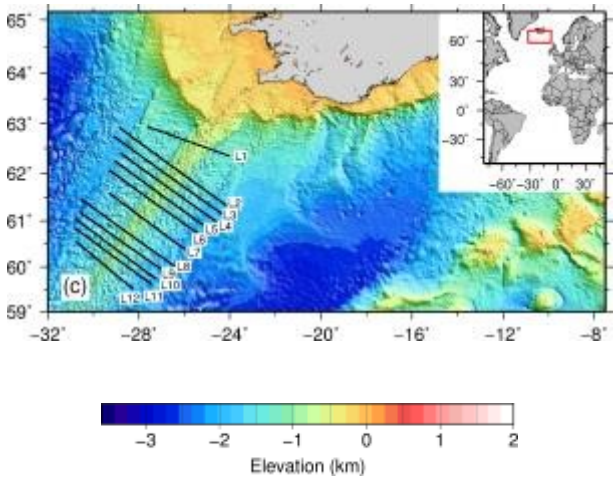

1021

1022

1023

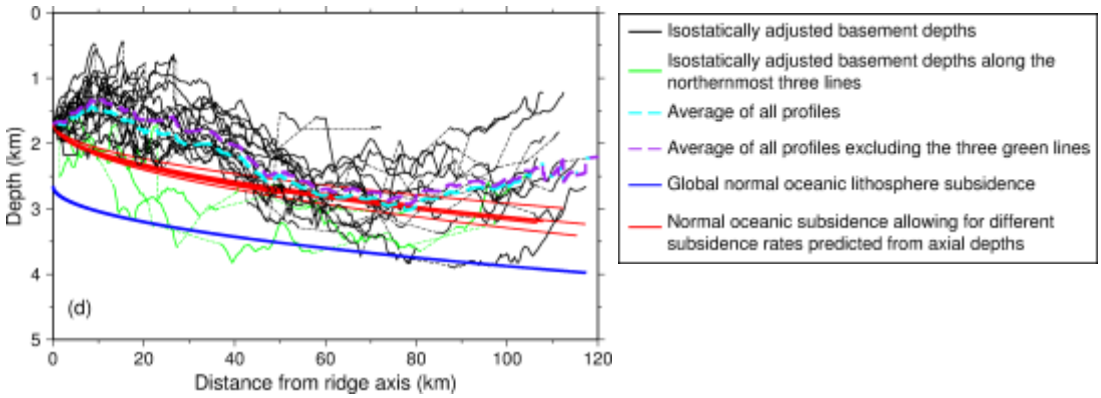

1024

1025 **Figure 5** (a): Basement depths along the Red Sea seismic lines (Figure 4) corrected for
1026 evaporite and other sediment loading. (b): Basement depths around the Reykjanes Ridge from
1027 Johansen et al. (1984), also corrected for sediment loading. (c): Locations of Reykjanes Ridge
1028 profiles shown over the bathymetry of Smith and Sandwell (1997, version 18.1). (d): Red Sea
1029 crustal deepening with distance from the ridge-axis. All profiles are shown offset to their
1030 average axial depth of 1.69 km (depth at zero distance). The solid blue line is the global normal
1031 oceanic lithosphere subsidence curve from Crosby and McKenzie (2009). Green lines are
1032 profiles 7 (both western and eastern flanks) and 9 (western flank) lying farthest from the Afar
1033 plume. Global normal oceanic lithosphere subsidence (blue line) was predicted from the
1034 Crosby and McKenzie (2009) rate with seafloor spreading rates from Chu and Gordon (1998).
1035 Normal oceanic subsidence curves allowing for different subsidence rates were predicted
1036 using the axial depths and the subsidence rates of Marty and Cazenave (1989). Red subsidence
1037 curves have been offset to common 1.69 km axial depth while blue subsidence curve is shown
1038 without offset.

1039

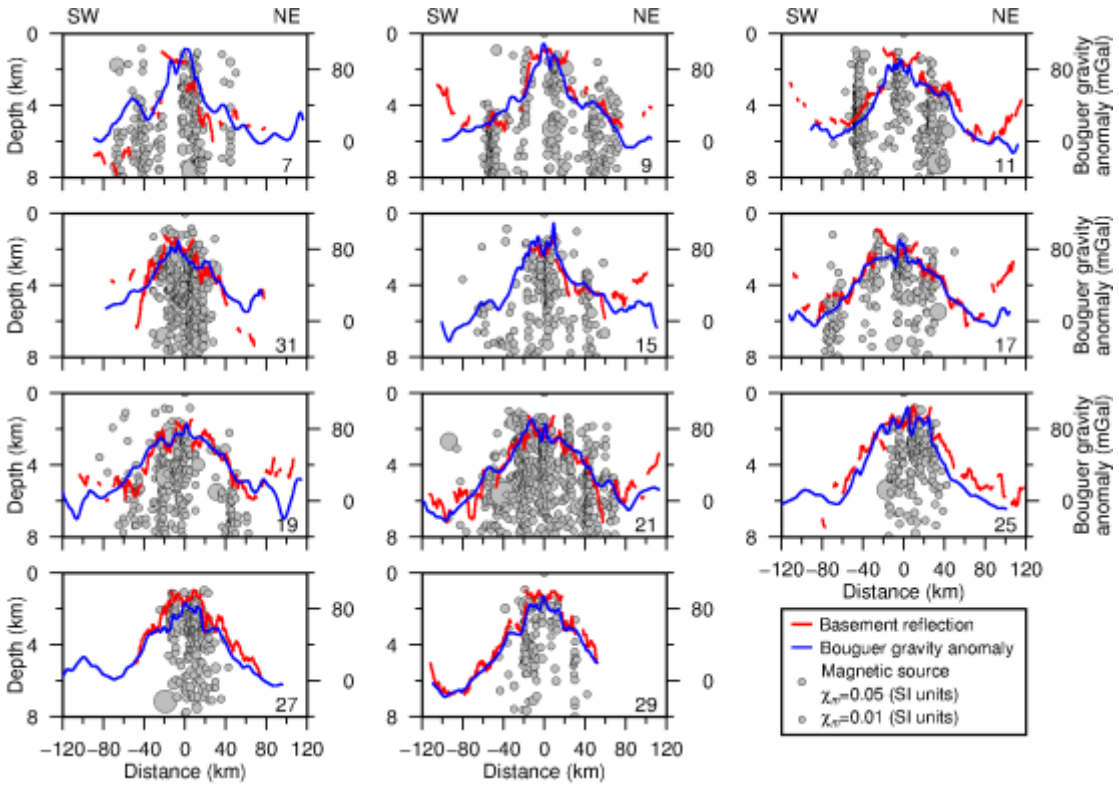

1040

1041 **Figure 6** Graphs showing correlation between basement reflection depths (red) and Bouguer

1042 gravity anomalies (blue) (Mitchell et al., 2017) derived by correcting free-air anomalies for

1043 seabed relief using a halite density (2160 kg m^{-3}). Line numbers are shown in lower right of

1044 each panel.

1045

1046

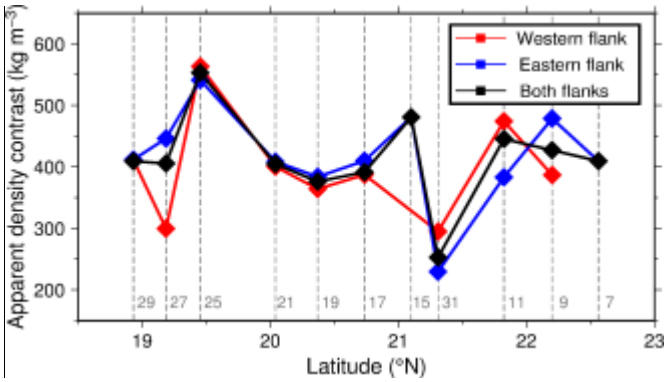

1047

1048 **Figure 7** Apparent density contrasts deduced from Bouguer-basement depth gradients. The
1049 red and blue symbols represent western and eastern flanks, while black symbols represent
1050 contrasts derived from data of both flanks combined. On the western flank of profile 7, the
1051 basement reflection was too indistinct to calculate an apparent density contrast.

1052

1053

1054

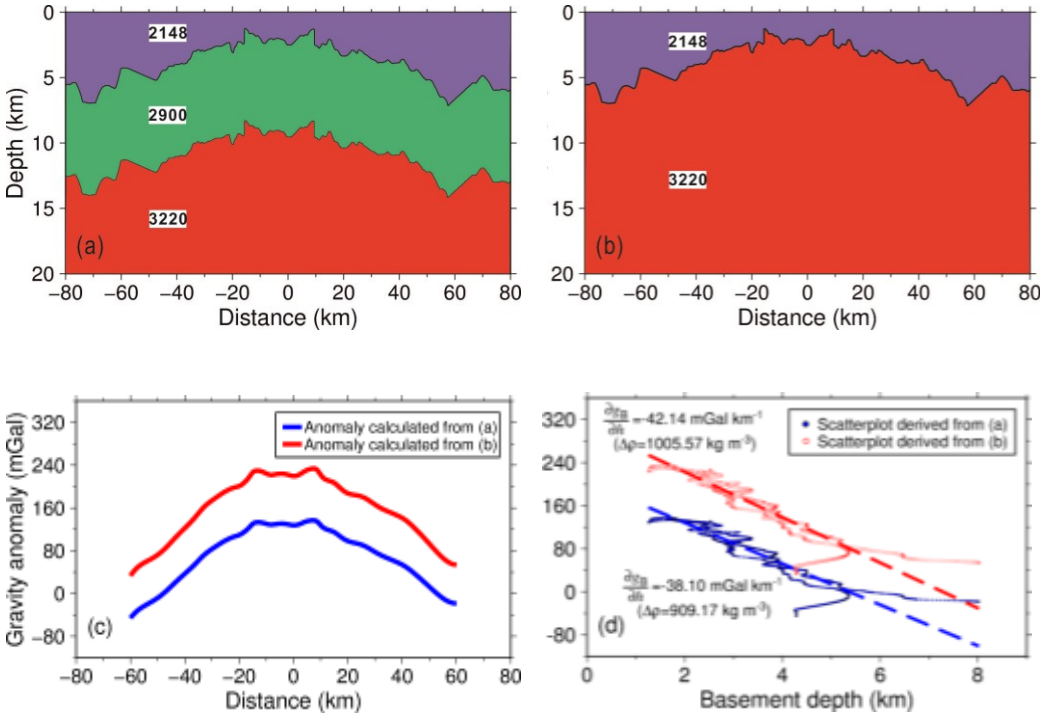

1055

1056 **Figure 8** Simulation using basement depth profile 21 illustrating how apparent density
1057 contrasts inferred using the gravity slab formula are reduced by upward continuation. (a):
1058 Model with evaporites (2148 kg m^{-3}), 7 km thick crust (2900 kg m^{-3}) and mantle (3220 kg m^{-3}).
1059 (b): Model with evaporites directly overlying mantle. (c): Theoretical Bouguer gravity
1060 anomalies computed using 2D gravity forward modelling for the two density models. (d):
1061 Scatterplots with regression lines of Bouguer gravity anomaly versus basement reflection
1062 depth. The slight difference in slope translates to a ~97 kg m^{-3} difference in apparent density
1063 contrast.

1064

1065

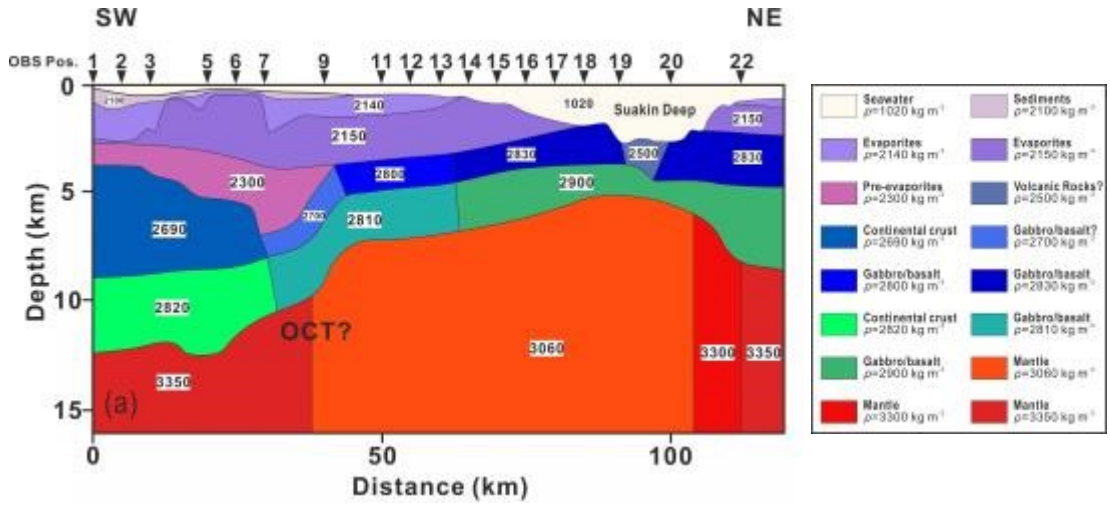

1066

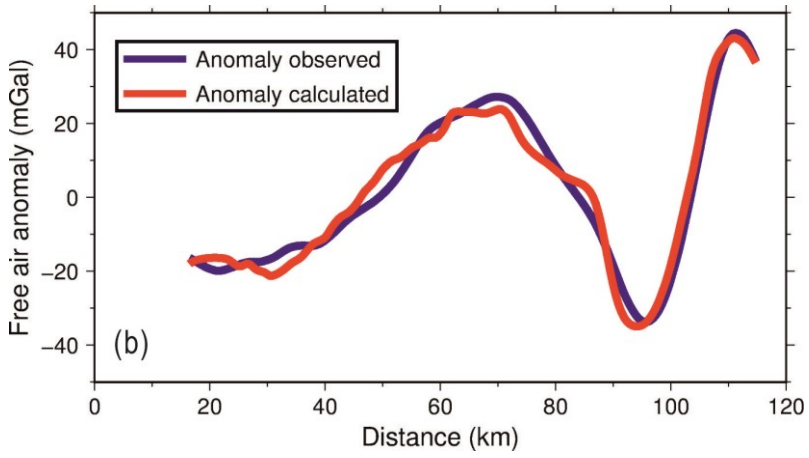

1067

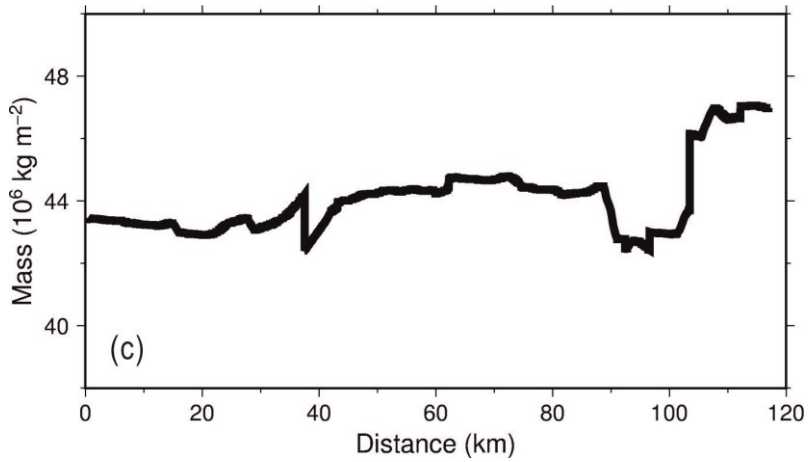

1068

1069 **Figure 9** (a): Density structure (kg m^{-3}) along line PIII line located in Figure 2 based on the
1070 seismic refraction velocity (V_p) model of Egloff et al. (1991, their profile SO53-PIII) and the
1071 density-velocity relations of Christensen and Shaw (1970). ("Pre-evaporites" are pre-evaporite

sedimentary rocks.) OCT: Oceanic–continental transition. (b): Free-air gravity anomaly calculated from (a) compared with observations from the Sandwell et al. (2014) gravity field (version 23.1). (c): Total mass anomaly per unit area along PIII, computed by integrating density over depth to the base of the model in (a).

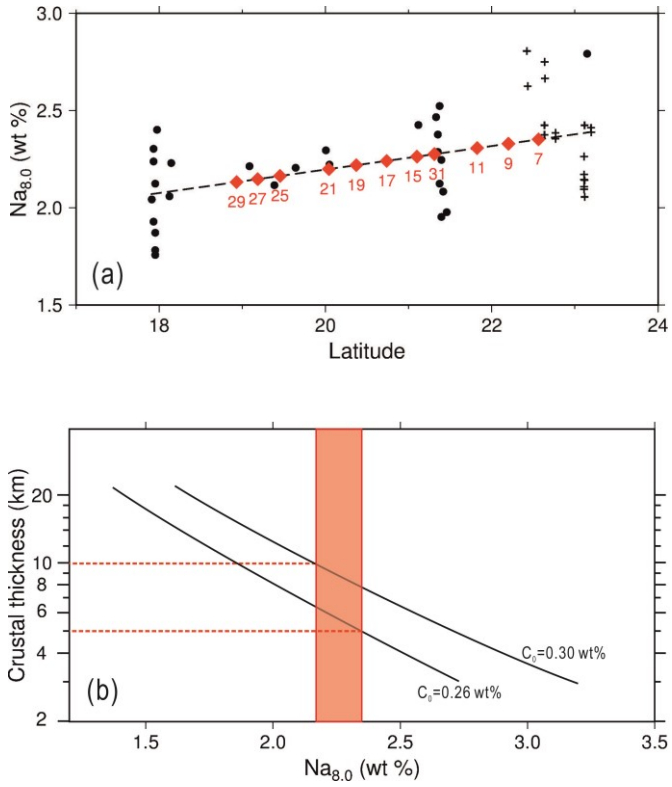

Figure 10 (a): Sodium oxide contents of axial lavas from Haase et al. (2000) (solid circles) and Ligi et al. (2012) (plus symbols) corrected for fractionation to 8 wt% MgO. Diamond symbols indicate the average $Na_{8.0}$ values expected at the axial locations of the eleven seismic reflection profiles based on the dashed regression line shown. (b): Seismically determined estimates of crustal thickness versus average $Na_{8.0}$ from Klein and Langmuir (1987). The $Na_{8.0}$ values at the seismic lines (orange shading) suggest that the axial crustal thickness of the central Red Sea is ~5-10 km (orange dashed lines).

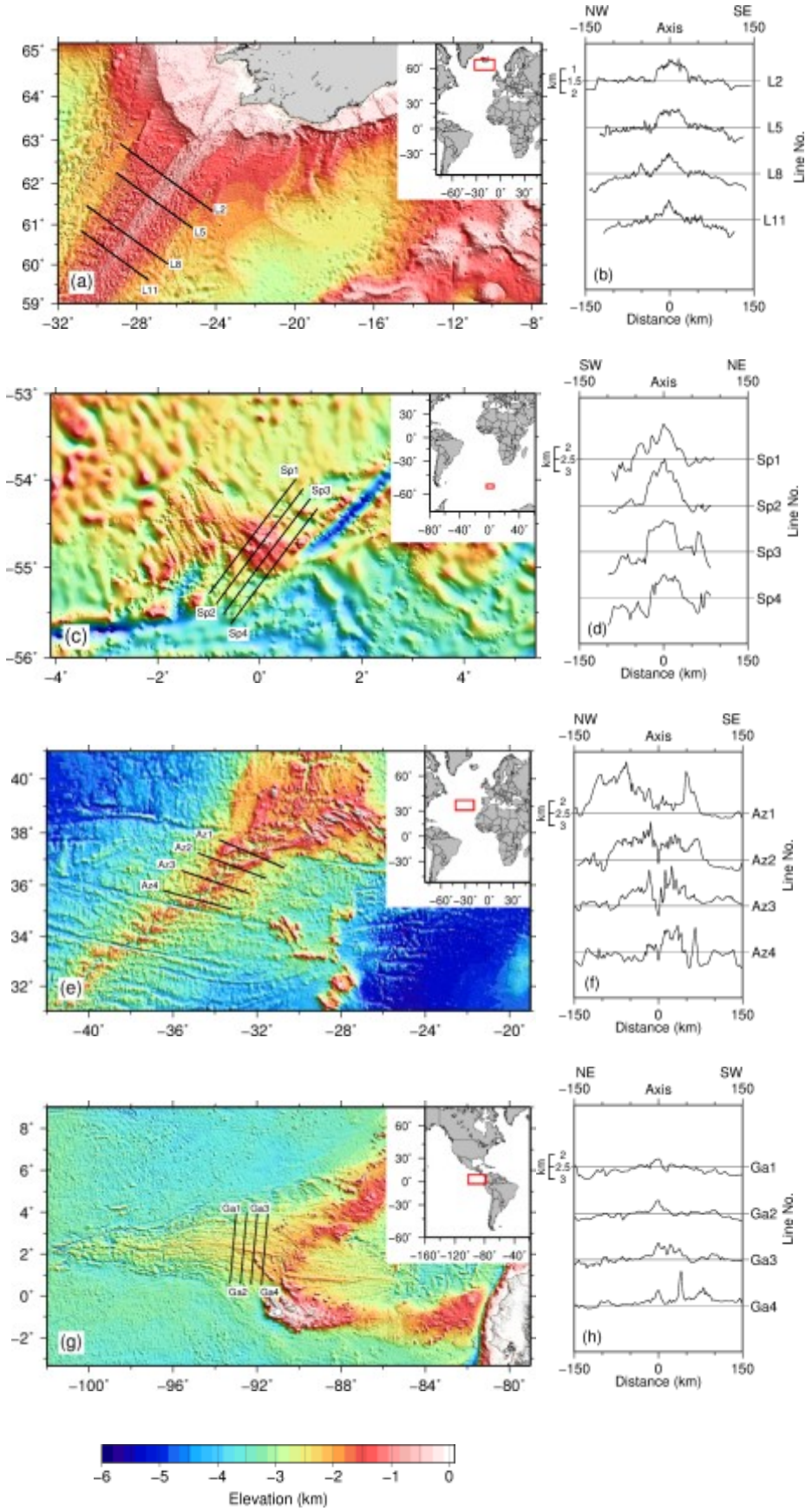
(a)
(b)
(c)
(d)
(e)
(f)
(g)
(h)
NW
SE
SW
NE
Axis
Distance (km)
Line No.
km
L2
L5
L8
L11
Sp1
Sp2
Sp3
Sp4
Az1
Az2
Az3
Az4
Ga1
Ga2
Ga3
Ga4
Elevation (km)

1092 **Figure 11** Examples of locally elevated topography at ridges located near mantle hotspots.
1093 Panels (a), (c), (e) and (g) locate profiles at the Reykjanes Ridge near the Iceland hotspot, the
1094 Spiess Ridge near the Bouvet hotspot, the northern Mid-Atlantic Ridge near Azores hotspot,
1095 and the Galápagos Spreading Centre near Galápagos hotspot, respectively. Panels (b), (d), (f),
1096 and (h) show the profiles located in (a), (c), (e) and (g), respectively. Bathymetry data from
1097 Smith and Sandwell (1997, version 18.1).

1098